UNIVERSITY OF WEST BOHEMIA

FACULTY OF APPLIED SCIENCES

DEPARTMENT OF PHYSICS

Master Thesis

Plzeň, 2015 Tomáš Vytisk

Reactive High Power Impulse Magnetron Sputtering of Vanadium Oxides

Declaration

I certify that this master thesis is my own work and it has not been published anywhere. All the sources have been quoted and acknowledged by means of complete references.

In Plzeň, 30.05.2015

Tomáš Vytisk

Acknowledgements

I would like to cordially thank all the people who enabled the creation of this thesis. That specially includes my supervisor Ing. Jiří Rezek, Ph.D. whom I greatly thank for his careful corrections and fitting comments. I also thank to a friend Ing. David Kolenatý, with whom I collaborated. It also involves all other stuff of the Department of Physics who creates friendly workplace for all the students. I deeply thank my family and close friends who supported me in all the ways during my studies.

Abstract

The aim of this thesis is to fabricate thermochromic thin film of vanadium oxide. High power impulse magnetron sputtering is used to prepare a thermochromic film with structure changes below transition temperature $\mathbf{T_c}$ = 68 °C providing variable transmittance in infrared spectrum. The films were prepared in oxygen and argon gas mixture, at pressure of working gas (Ar) $\mathbf{p_{ar}}$ = 1.0 Pa. A vanadium target (99.999 %) of 50 mm in diameter was loaded by average power density during deposition $\mathbf{<S_d>}$ = 12.4 – 14.0 W/cm^2. Other deposition parameters were: voltage pulse length $\mathbf{t_1}$ = 40, 50 and 80 μs with power supply repetition frequency **f** = 250, 200 a 125 Hz, respectively. Duty cycle was constant 1 %. The thin films were sputtered on glass and silicone substrates with orientation (100). Substrates were mounted on a substrate holder with possibility of heating. The holder was placed in 150 mm from the target. Reactive gas (O_2) was delivered to the deposition chamber through a corundum tube that was situated 20 mm above the target. A significant deposition parameter was substrate temperature **T** and deposition time **t**. The substrate temperature was **T** = 400 °C or **T** < 40 °C. XRD and Raman analyses were accomplished at the films in order to investigate their structure. Ellipsometry was used to measure optical characteristics $\Delta\mathbf{\Psi(\lambda)}$ and parameters like refraction index **n** and extinction coefficient **k**. This work presents an influence of deposition parameters (voltage pulse length $\mathbf{t_1}$, substrate temperature **T** and deposition time **t**) on thermochromic behaviour of the thin films. Thermochromic properties of the films are described by a change of ellipsometric angle $\Delta\mathbf{\Psi}$.

Key words: HiPIMS, vanadium oxide, reactive magnetron sputtering, thermochromic thin films

Abstrakt

Tato práce je zaměřena na vysokovýkonovou pulzní magnetronovou depozici tenkých vrstev oxidu vanadu. Cílem je vytvořit termochromickou vrstvu oxidu vanadu, jejíž přechodová teplota bude nižší než 68 °C a bude vykazovat změny propustnosti v oblasti infračerveného záření. Vrstvy byly připravovány v plynné směsi argonu a kyslíku za konstantního tlaku pracovního plynu $\mathbf{p_{ar}}$ = 1.0 Pa. Vanadiový terč (99.999 %) o průměru 50 mm byl zatěžován průměrnou výkonovou hustotou při depozici $\mathbf{<S_d>}$ = 12.4 – 14.0 W/cm^2. Délka trvání pulzu byla $\mathbf{t_1}$ = 40, 50 a 80 μs s opakovací frekvencí napájecího zdroje **f** = 250, 200 a 125 Hz, dle uvedeného pořadí. Střída byla konstantní 1 %. Vrstvy byly nanášeny na sklo a křemíkový substrát Si s orientací (100), které byly umístěné na vyhřívaném držáku ve vzdálenosti 150 mm od terče. Reaktivní plyn (O_2) byl přiváděn do depoziční komory korundovou trubičkou umístěnou 20 mm nad terčem. Významným depozičním parametrem je teplota vyhřívání substrátu **T** a délka depozičního procesu **t**. Teplota vyhřívání byla buď 400 °C nebo rovna okolní teplotě prostředí < 40 °C. U takto připravených vrstev byla provedena RTG strukturní a fázová analýza a Ramanova spektrometrická analýza strukturních vazeb v materiálu. Pomocí elipsometrie byla zjištěna tloušťka deponovaných vrstev a zkoumány optické parametry jako index lomu **n** a extinkční koeficient **k.** V této práci jsou prezentovány výsledky vlivu depozičních parametrů, zejména délky trvání pulzu $\mathbf{t_1}$, teploty substrátu **T** a délky depozičního procesu **t** (tloušťky vrstvy) na termochromické vlastnosti připravených vrstev. Termochromické chování je popsáno změnou elipsometrického úhlu $\Delta\Psi$ v závislosti na vlnové délce záření a teploty zkoumané vrstvy.

Klíčová slova: HiPIMS, oxid vanadu, reaktivní magnetronové naprašování, termochomické vrstvy

CONTENTS

CHAPTER 1: INTRODUCTION

1.1 MOTIVATION AND CHALLENGES

Nowadays energy consumption becomes a global problem. Increasing demand for energy gains the importance in the modern world. This causes an effort to explore new efficient ways to save energy. Innovation of thermal insulation has made great progress in last decades. The latest modern buildings manage thermal energy very smartly. However there is still a weak point in the thermal insulation – windows.

1.2 POSSIBLE SOLUTIONS

Modern solutions to the control energy demand involve the use of efficient systems or methods. Thin films for solar control offer possible glazing solutions. There are three main types of static metal oxide films: low emissivity films, heat mirrors (spectrally selective films) or absorbing layers. This work focuses on spectrally selective films – termochromic coatings. Basic principle of thermochromic materials is displayed in figure 1. Farther potential of thermochromism is in laser marking, warning signals, thermal sensors for safety, liquid crystals and inorganic oxides.[1]

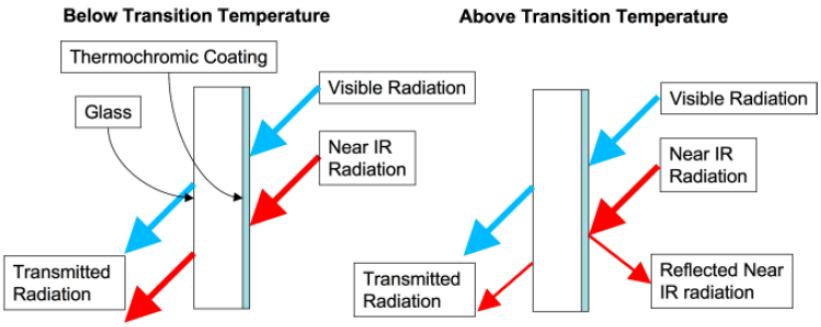

Fig. 1: Schematic representation of thermochromic materials applied as an intelligent window coating.[2]

CHAPTER 2: STATE OF THE ART

2.1 THEORETICAL BACKGROUND OF THERMOCHROMISM

Principal characteristic of thermochromic material is an ability to change colour upon reaching a certain temperature. This transition temperature affects the structure of material thereby optical and electrical properties. Typically the transition temperature occurs in a range of temperatures, which is observed as continuous thermochromism. Nevertheless discontinuous thermochromism can be found as well. There are two orders of phase transition in respect of thermodynamic potential **G**, where **G** is Gibbs free energy. If the first derivate of **G** is discontinuous the transition is called "first order". When the derivation is continuous and the second derivate of **G** is discontinuous, it is considered as "second order". In general this temperature-dependant transition is known as semiconductor to metal transition, which is described by many models.[1]

Free electron model describes distinction between metals and non-metals. However, the findings of transition-metal oxides showed inadequacy of this model. This is caused by absence of electron-electron interaction. By contrast, one band model describes semiconductor-to-metal transition by imagining a crystalline array of one-electron atoms with a variable lattice constant **b**. At large values of **b** the material would be insulating, since activation energy is required to form a pair of carries. As **b** becomes smaller so the activation energy decreases. At a certain value of **b**, a drop in activation energy is discontinuous transition. Figure 2 illustrates the principle of one band model.[3]

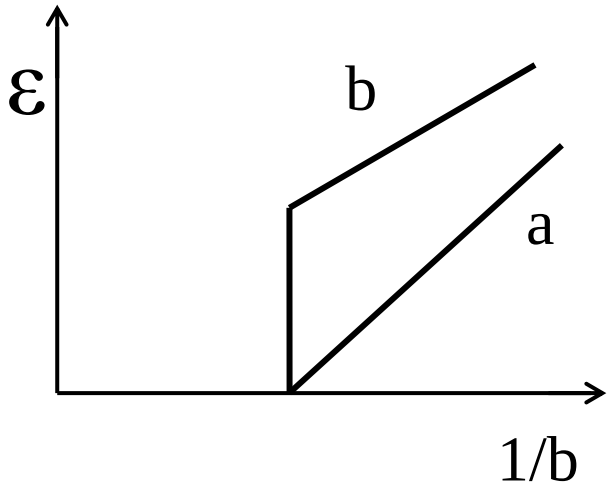

Fig. 2: The change of activation energy versus reciprocal lattice constant. (a) shows a continuous change and (b) shows a discontinuous change.[2]

A different approach is explained in [4]. There is proposed a two band model. When splitting of d-band at Néel temperature (Néel temperature is a characteristic for each antiferromagnetic material when above this temperature spontaneous antiparallel coupling of atomic magnets is disrupted and disappears) it influences insulating properties of the ground state in antiferromagnetic transition-metal materials. This allows all bands to be full or empty. Therefore it is antiferromagnetic ordering that leads to the insulating nature. For all that two band model has never been quantitatively applied to the vanadium or titanium oxides.

Another possible way to explain the nature of semiconductor-to-metal transition is change in crystal structure. This change leads to formation of the band gap as well.

2.2 THERMOCHROMIC TRANSITION METAL OXIDES

Since metals are characterized by a low resistivity (10^{-2} – 10^{-6} Ωcm) at ambient temperature and its resistivity increases linearly with temperature. Semiconductors and insulators have higher values of resistivity (10^{3} – 10^{17} Ωcm) at room temperature. That values decrease exponentially with rising temperature. Transition metal oxides such as Ti_2O_3, V_20_5, VO_2 and VO are all semiconducting at low temperatures and show abrupt transition at the Néel temperature. Due to continuity of electrical and optical properties, it is relevant to observe both characters of transition metal oxides.

Vanadium oxides are the most investigated transition metal oxides at the present time, due to their extraordinary electronic, structural, magnetic and optical behaviour, particularly VO_2 and V_2O_5.

Vanadium oxide (VO_2) is the most studied solid-state thermochromic material. The transition temperature of a pure single crystal is 68°C. Below this temperature a monoclinic structure phase is stable. At ambient temperature the lattice unit cell parameters are a = 5.75 Å, b = 4.52 Å, c = 5.38 Å, β = 122.60°. After passing the transition temperature the monoclinic phase changes to a high temperature rutile lattice, the cell parameters are a = 4.55 Å, c = 2.85 Å. The monoclinic structure behaves as a semiconductor compared to the rutile phase with semimetal properties. The two vanadium oxides structures can be seen in figure 3. [2]

The nature of this semiconductor-to-metal transition and the two phases was explained by Goodenough [5]. The model is based on molecular orbitals and a band structure diagram shown in figure 4. The band scheme displays d_{II} orbitals in monoclinic structure, resulting from overlap of atomic orbitals in V^{4+}-V^{4+} pairing. During the transition from monoclinic to rutile phase, the (100) planes of vanadium atoms shift by 0.043 nm parallel to (001). This shift causes the breaking of the V^{4+}-V^{4+} pairs to form the tetragonal phase, allowing metal conductivity. An antiferroelectric transition is proposed as driving force for the semiconductor-to-metal transition. According to this theory the antiferroelectric and the crystallographic distortion are significant processes giving vanadium oxide such a promising potential. In spite of the theory, semiconductor-to-metal transition is not fully understood by far. [1][6]

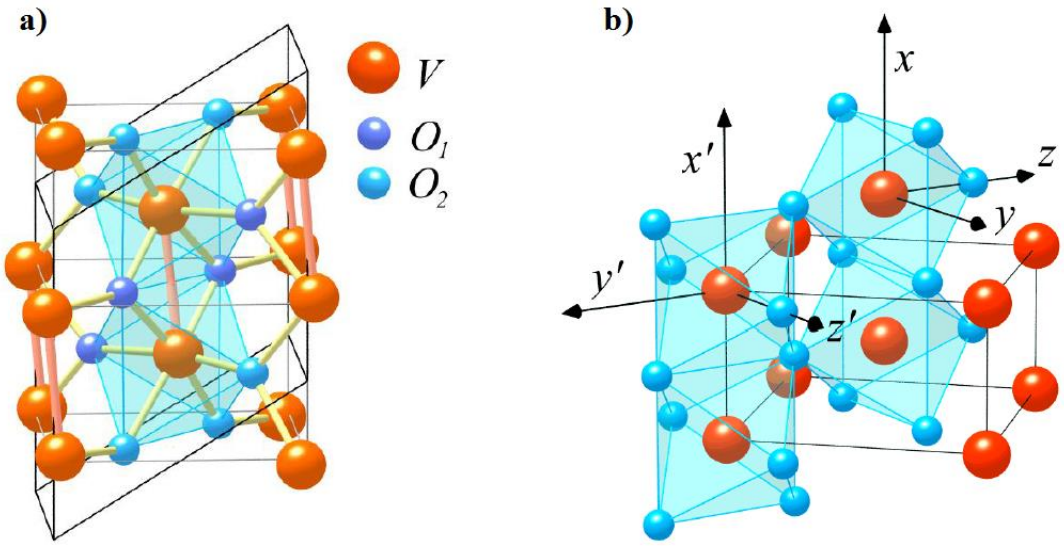

Fig. 3: (a) monoclinic structure of VO_2 when $T<T_c$.(b) rutile structure when $T>T_c$.[6]

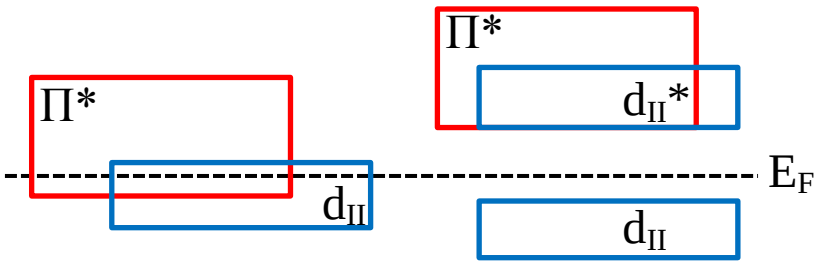

(a) Tetragonal (b) Monoclinic

Fig. 4: Electronic band diagram for vanadium oxide. [5]

Going from one phase to the other, can be seen a hysteresis behaviour, which is typical feature of first order transition. This happens when some parts of the material already went thought the transition while the others did not.

Vanadium pentoxide V_2O_5 also exhibits thermochromic behaviour. Its transition temperature is 257 °C. In the semiconductor state ($T < T_c$) the structure is orthorhombic, composed of corner and edge sharing VO_6 octahedras. Lattice parameters of the orthorhombic unit cell are a = 11.510 Å, b = 3.563 Å, c = 4.369 Å.[7] Due to long distance V-O in c-axis, can be the structure described by pyramids of VO_5 (figure 5). This is typical for all other thermochromic materials. Orthorhombic structure is made of zig-zag pyramidal VO_5 units. There is a variety of technique preparations of oxides of vanadium such as CVD, PVD, sol-gel-method,

pulsed laser deposition and evaporation. In thin film form vanadium pentoxide offers the possibility of integration into micro-electronic circuitry and optoelectronic devices.[8]

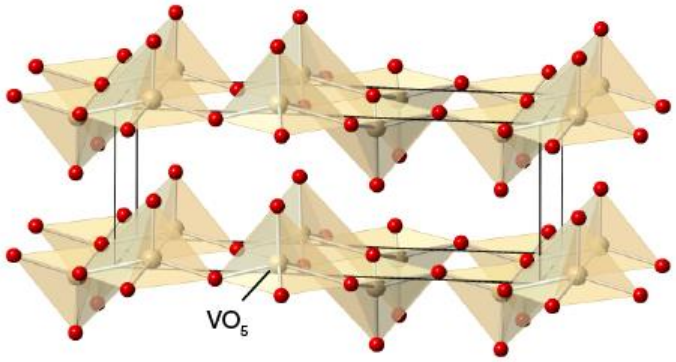

Fig. 5: The orthorhombic structure of V_2O_5.[7]

2.3 State of Research

This section examines possible methods of preparation of vanadium oxide films and their characterization and obtained results so far.

2.3.1 Electrical Properties of VO_2 Thin Films

F. Guinneton et al. [9] compare nanocrystalline powder and thin films of vanadium dioxide. Stable Rutile form of vanadium dioxide was obtained by placing metastable precursor VO_2 in a quartz crucible, heated under inert atmosphere. Thin films of vanadium dioxide were prepared by RF reactive sputtering. The thin films were deposited on an amorphous silica substrate using a pure metallic vanadium target (HTC, purity 99.7%). The electrical resistance was analysed using a four-points equipment associated with a Hewlett Packard HP 3456A multimeter, and using a Peltier device coupled with an automated control temperature (rate 28 C/min). Results of electrical measurements are reported in figure 6. One can see the shift of transition temperature of compacted powders samples to higher value. This shift is probably caused by heating from the support (below face) and that a significant thermal gradient is probably involved in presented experiments.

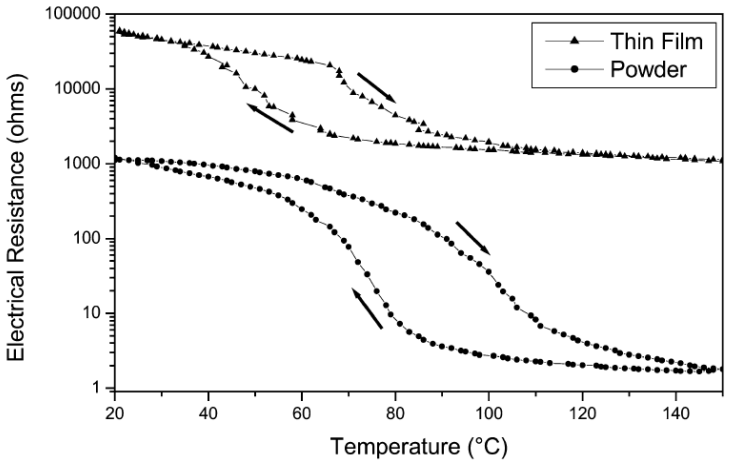

Fig.6: Electrical resistance of compacted nanopowder and thin film of thermochromic VO_2 versus temperature. [9]

The measured resistances of the thin film and of the compacted powder sample are highly different. Resistance **R** of thin film at 20 °C is **R** = 70 kΩ while the compacted sample presents a lower resistance of **R** = 1050 Ω. At 140 °C, above the transition temperature, the resistances fall to **R** = 2 kΩ and **R** = 5 Ω, respectively, for the thin film and compacted samples. Activation energies are 0.162 eV (±0.002 eV) and 0.129 eV (±0.006 eV), respectively, for thin film and powder sample. This shows that the thin film is more resistive than the compacted powder samples. Explanation of the difference in the activation energies can be interpreted in terms of improved electrical contacts between grains in the compacted sample. A simple model can be introduced when measured resistance is compound of VO_2 resistance and interfaces. Using the experimental date of figure 6 the interface resistance in the thin films is evaluated **R** = 1675 Ω.

Another comparative study [10] focuses on vanadium dioxide films, which were prepared by DC and rf reactive magnetron sputtering of a 99.7% pure vanadium target. Deposition was accomplished in Ar and O_2 plasma with a well-controlled oxygen partial pressure. The films were deposited onto normal glass substrates at 400 °C. The films showed a metal-semiconductor transition at the temperature between 65 – 68 °C. The sheet resistance, $\mathbf{R_s}$, defined as resistance/square area was measured by pressing a two-point probe against the film.

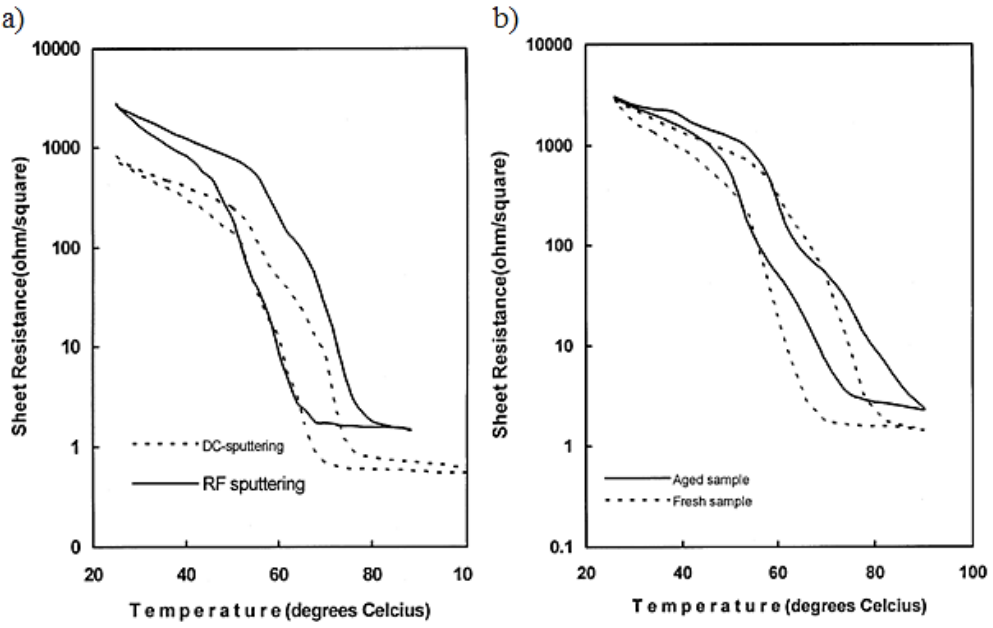

Fig. 7:a) Sheet resistance versus temperature for a) DC and rf sputtered VO_2 films; b)fresh and aged sample [10].

For the rf sputtered VO_2 films, the sheet resistance displayed in figure 7 (a) shows a jump of about 10^3 ohm/ square and a hysteresis width of 12 °C. The oxygen flow rate was 2.85 sccm and the thickness of the film was 700 nm. DC sputtered film was 280 nm thick, prepared using oxygen flow rate of 4.6 sccm shows the same sheet resistance jump 10^3 and hysteresis width of about 8 °C. Referred VO_2 films, made by rf sputtering, were observed after 12 months to determine again the effect of the films. As figure 7 (b) shows the jump in sheet resistance was found to be basically same for both cases. [10]

2.3.2 Spectral Properties of VO_2 Thin Films

It should be mentioned in context of optical transmittance that the transmittance is a function of thickness. This is described by Beer-Lambert law

$$T = e^{-\sigma N l}. \tag{2.1}$$

Where **T** is the transmittance, **N** is the number density of the attenuating species in the material, **l** is the path length and **σ** is the attenuation cross section. Vanadium dioxide is slightly absorbing in the visible spectra (a fine coloring of film). Therefore a small thickness results in high transmission at low temperature in visible spectra as well as in the infrared at high temperature state. On the other side, higher

thickness of layer causes low transmission at low temperature in visible spectra and in the infrared at high temperature state. Thus it is necessary to find a compromise of the referred effects.[11]

Optical properties of vanadium dioxide belong to the most monitored characteristics in the research of thermochromic materials. A recent study [12] investigates the optical properties of VO_2 sputtered by HiPIMS. As the authors explain HiPIMS brings promising possibilities for fabrication of polycrystalline thermochromic coatings. The films were deposited onto glass placed at 15 cm from the target and heated up to 300 °C. Parameters of deposition were follow: a working pressure of 1.33 Pa, an oxygen-to-argon flow ratio of 0.06 at a voltage pulse length of 45 μs, a pulse frequency of 200 Hz and a pulse peak voltage of 900 V. The selected thickness of the film was 75 nm and 185 nm. Spectral transmittance of 75 nm film is shown in figure 8. Normal incidence spectral transmittance **T** of VO_2 films was obtained at different temperatures using a Perkin Elmer Lambda 19 spectrophotometer for wavelengths ranging from 400 to 2500 nm. As it is shown in figure 8 the difference of transmittance at wavelength 2500 nm is 61 % for temperatures below and above transition temperature. Figure 9 displays the hysteresis of 75 nm and 185 nm thick VO_2 films. The abrupt switching behavior can be correlated to the high crystallinity and large grain size, which are determined by XRD and AFM right in [12]. The transition temperatures 50 °C (185 nm) and 63 °C (75 nm) are lower than for bulk material (68 °C). This shift of transition temperature can be explained by mechanical stress in the films. In fact, the stronger densification so reducing V–V distance in crystalline structure results in a direct overlap of d orbitals thus stabilize metallic phase at lower temperatures.

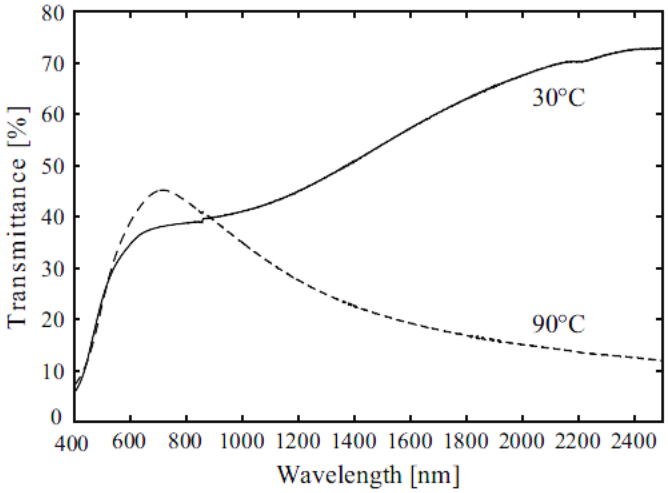

Fig. 8: Optical transmittance of a 75 nm thick VO_2 film as a function of wavelength at 30 °C and 90 °C.[12]

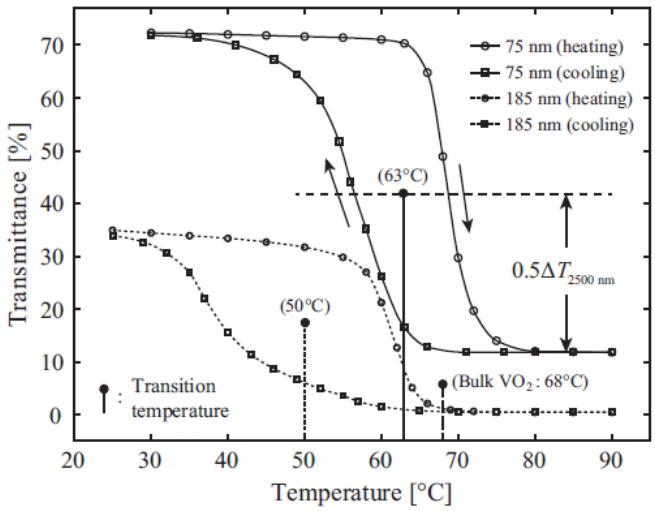

Fig. 9: Transmittance hysteresis at 2500 nm of two VO_2 samples possessing different thicknesses (75 nm and 185 nm).[12]

An alternative method of lowering transition temperature $\mathbf{T_c}$ is investigated in [13]. The paper presents an influence of tungsten doping content in sputtered VO_2 films. The samples were prepared by reactive dc magnetron sputtering of two targets made of tungsten (purity 99.95 %) and vanadium (purity 99.7 %). Power on the V target and W target was 250 W and 0 – 6 W respectively. Gas pressure was 1.01 Pa. Substrate temperature 400 °C and current on W target 0 – 0.016 A. The sputtered films show a drop of the transition temperature with increasing tungsten doping However, tungsten doping alone does not provide an acceptable color of the VO_2 films [14]. By co-doping vanadium oxide with tungsten and fluorine, films can be

obtained with the desired transition temperature, as well as improved transmittance in the visible spectral range. Figure 10 illustrates the influence (reducing) of tungsten and fluorine doping on transition temperature.[14] Further, there can be used another doping element such as Mo.[15]

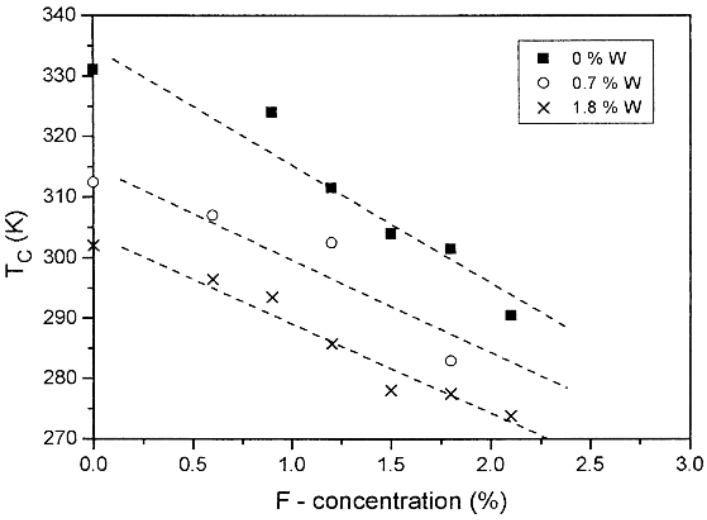

Fig. 10: Transition temperature T_C of doped VO_2 films. T is reduced due to fluorine and tungsten incorporation. The effect is less pronounced in co-doped samples compared to single-element doping.[14]

With ammonium molybdate and ammonium tungstate as precursors, Mo and W co-doped VO_2 films were fabricated on muscovite (001) substrate by the aqueous sol-gel method. The $\mathbf{T_c}$ decreasing of the Mo-W co-doped vanadium dioxide film is not the superposition of the respective influence of each single ion doping, and the $\mathbf{T_c}$ of co-doped films is lower than that of single Mo doped VO_2 film at the same doping level. Prepared films $V_{1-x-y}Mo_xW_yO_2$ (x = 0.5 at.%, y = 0.25 at.%) exhibit transition temperature reduced to 36 °C.[15]

The work of Jing Du et al. [16] studies a behavior of vanadium dioxide films doped by Ti. The authors found relation between content of titanium in the films and width of hysteresis loop shown in figure 11. The synthesis of Ti-doped VO_2 films was realized by polymer-assisted deposition (PAD). Prepared films show denser morphology and smaller particles while increasing content of Ti in the films. The rise of doping concentration increases density of defect-induced nucleation sites. As a result of that the width of hysteresis loop is reduced. The results of this work correspond with results in [17], where the authors indicated a positive influence of increasing W-doping concentration on width of hysteresis loop as well.

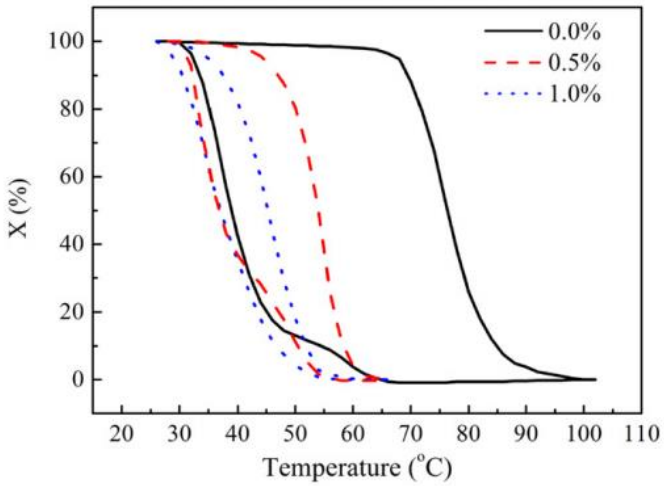

Fig.11: Normalized transmittance X of thermal hysteresis of Ti-doped VO_2 films.[16]

2.3.3 MORPHOLOGY OF VO_2 THIN FILMS

As mentioned in the previous section, morphology of fabricated thin films plays a significant role in properties of vanadium dioxide films. It was already noted that doping concentration affects the structure of the films. Referring to the work [16] increasing content of Ti makes the films denser. This influence can be easily observed in figure 12. The morphology of the films was determined by field emission scanning electron microscopy (FESEM). As Ti content x increased, the films obviously became denser and the particles became smaller. The mean particle diameter decreased from 130 nm (x = 0.000) to 30 nm (x = 0.091). Densification of VO_2 films provides possibility decreasing of transition temperature and width of hysteresis loop. The research [18] explains the shift of transition temperature and the varying width of the hysteresis loop. When the distance between vanadium atoms decreases, it results in a direct overlap of d orbitals, which increases the width of the d band and stabilizes the metallic phase of the rutile structure. As seen in figure 13 an intimate relation is suggested, transition temperatures become low in the films with smaller lattice parameter c.

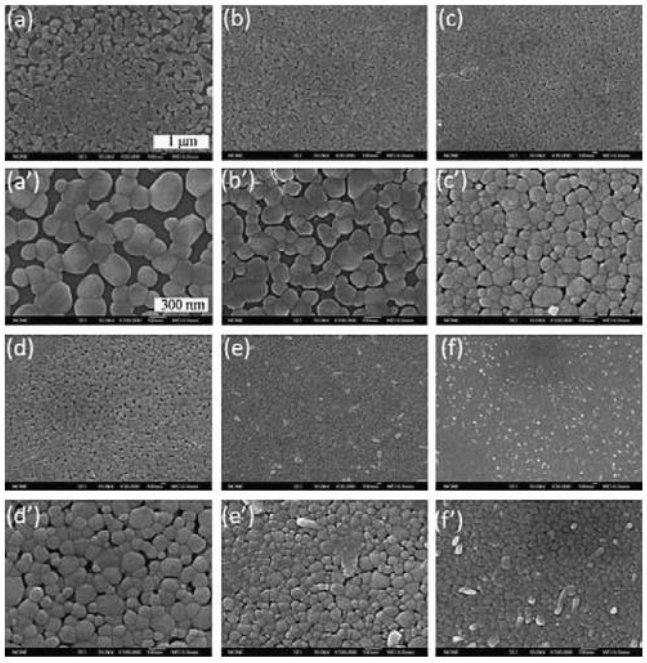

Fig. 12: FESEM photographs of Ti-doped VO_2 films with different Ti contents. (a)/(a′) = 0, (b)/(b′) = 0.02, (c)/(c′) = 0.038, (d)/(d′) = 0.057, (e)/(e′) = 0.074, (f)/(f′) = 0.091.The scale bar for (a)- (f) and (a′) – (f′) is shown in (a) and (a′)respectively.[16]

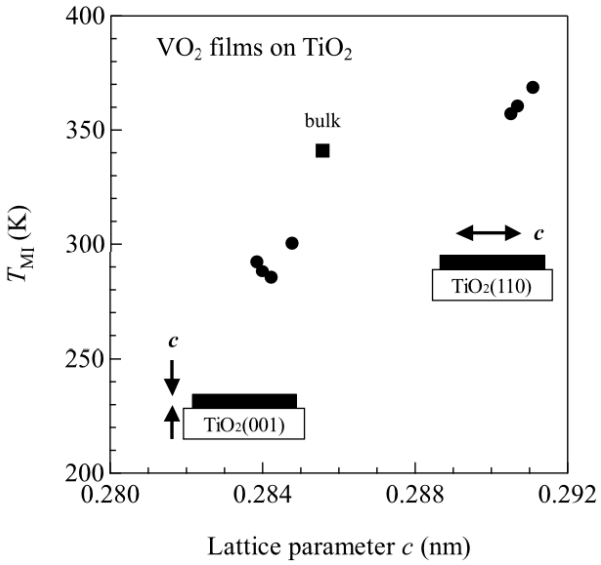

Fig. 13: Transition temperature T_{MI} as a function of lattice parameter c for the VO_2 films deposited on (a) TiO_2 (001) and (b) on TiO_2 (110) substrates. The single crystal VO_2 data is plotted – bulk material. [18]

2.4 METHODS OF THIN FILM DEPOSITION

Physical Vapour Deposition (PVD) processes are atomistic deposition processes in which material is transported from a solid or liquid source, in the form of atoms or molecules, to the substrate where it condenses. Most of the PVD processes are accomplished in plasma environment, by energetic ion bombardment of a solid surface. Fundamental deposition techniques are DC and RF sputtering, which lay the foundation of modern and perspective techniques such as HIPIMS (High Power Impulse Magnetron Sputtering) or other hybrid or modified processes.

2.4.1 MAGNETRON SPUTTERING

Magnetron sputtering is based on actuating of electric field $\vec{\mathbf{E}}$ and magnetic field $\vec{\mathbf{B}}$ on electron motion. Electrons within the dual field environment experience the well-known Lorentz force in addition to electric field force, i.e.

$$\vec{F} = \frac{md\vec{v}}{dt} = -q\left(\vec{E} + \vec{v} \times \vec{B}\right), \tag{2.2}$$

where $\vec{\mathbf{v}}$, **q** and **m** are the electron velocity, charge and mass, respectively. First consider $\vec{\mathbf{B}} \parallel \vec{\mathbf{E}} \parallel \vec{\mathbf{v}}$ therefore emitted electron is influenced only by the electric field, which accelerates it. In the case of the neglected electric field and the applied magnetic field $\vec{\mathbf{B}}$ the situation changes. A launched electron at angle **Θ** with respect to $\vec{\mathbf{B}}$ travels in a spiral motion with constant radius **r** and cyclotron frequency **ω**, i.e.

$$r = \frac{mvsin(\Theta)}{q\vec{B}} \tag{2.3}$$

$$\omega = \frac{qB}{m} \tag{2.4}$$

The case, where electrons are launched at an angle to parallel, uniform $\vec{\mathbf{E}}$ and $\vec{\mathbf{B}}$, is somewhat more complex. Spiral motion occurs but not always with constant radius. All the three cases are shown in figure 14. [19] The invention of magnetic sputtering is credited to J. S. Chapin (1979). He opened a new area in vacuum coating technology. The main advantages of magnetron sputtering are as: low plasma impedance and thus high discharge currents, deposition rates in the range from1 nm/s to10 nm/s, dense and well adherent coatings and broadly tunable film properties.[20]

Essentially magnetron is a configuration of permanent magnets situated on the target in a sputtering chamber. Magnetrons are classified into two types as shown in figure 15. In a conventional magnetron the plasma is strongly confined to the target region. Films grow on substrate that is placed out of high plasma density region. Consequently, the ion current drawn at the substrate is generally insufficient to modify the structure of the film. In an unbalanced magnetron the outer circle of magnets is strengthened relative to the central pole. Hence, not all the magnetic lines are closed between the central and outer poles in the magnetron, but some are directed towards the substrate, and some secondary electrons are able to follow these lines. Electrons accomplish more collisions on their way towards the substrate, thus ion current is higher than in conventional magnetron. [21]

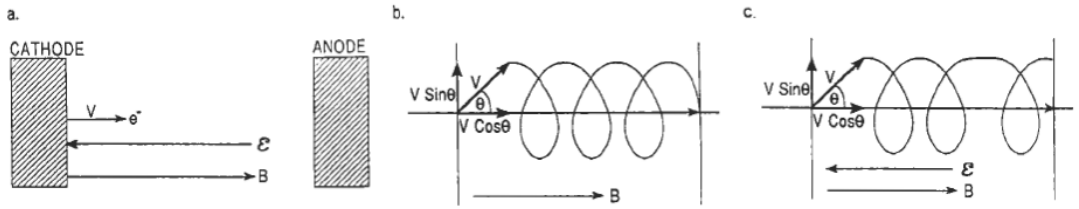

Fig. 14: Effect of electric and magnetic field on electron motion. (a)Linear electron trajectory when $\vec{B} \parallel \vec{E} \parallel \vec{v}$ *and* $\Theta = 0$*.(b)Spiral trajectory with constant radius when* $\vec{E} = 0, \Theta \neq 0$*.(c)Spiral motion with variable radius when* $\vec{B} \parallel \vec{E} \neq 0$ *and* $\Theta \neq 0$*.*[19]

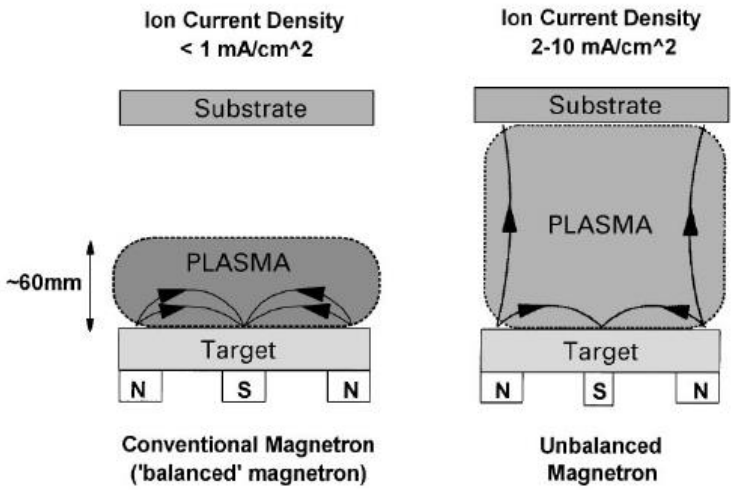

Fig. 15: Schematic presentation of balanced and unbalanced magnetrons.[21]

Thanks to inhomogeneous magnetic and electric field, a specific drift occurs in electron motion. This is known as the $\vec{\mathbf{E}} \times \vec{\mathbf{B}}$ drift. One could notice that the magnetically closed $\vec{\mathbf{E}} \times \vec{\mathbf{B}}$ drift is also described as the Hall current.[22]

Planar magnetron is frequently used configuration in plasma sputtering, displayed in figure 16. Along the electron trajectories an erosion zone - racetrack can be observed, where increased plasma density evokes a higher sputter yield. Therefore commercial magnetrons improve the utilization of targets by using so-called interpoles target-hollow magnetron, for instance.[20]

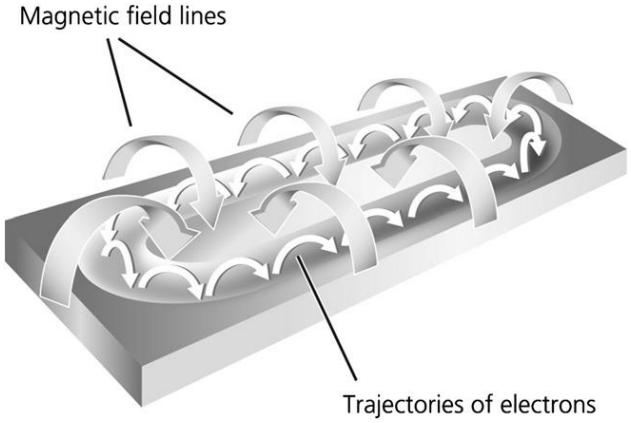

Fig. 16: Electron motion and erosion zone at planar magnetron.[20]

2.4.2 Reactive Sputtering

Reactive sputtering is a deposition process, where the deposited film is formed by chemical reaction between the target material atoms and gas atoms. This reactive gas flows to the deposition chamber with the working gas collectively. The chemical composition formed on the substrate can be controlled by relative pressure of inert and reactive gas. Oxide and nitride films are often fabricated by using this method. During a reactive sputtering process, the reaction between the target material and the reactive gas might lead to process instability due to several effects. The most common among these are: hysteresis, arcing and disappearing anode.[23]

2.4.2.1 Hysteresis

During variable reactive gas flow hysteresis effect is commonly observed. In presumption of metallic target, the principal of hysteresis effect is shown in figure 17. Increasing flow of the reactive gas does not influence total pressure in the deposition chamber until reaching critical gas flow (A). In this situation all

atoms of the reactive gas react with sputtered atoms, substrate or walls of chamber. This is called a metal mode.

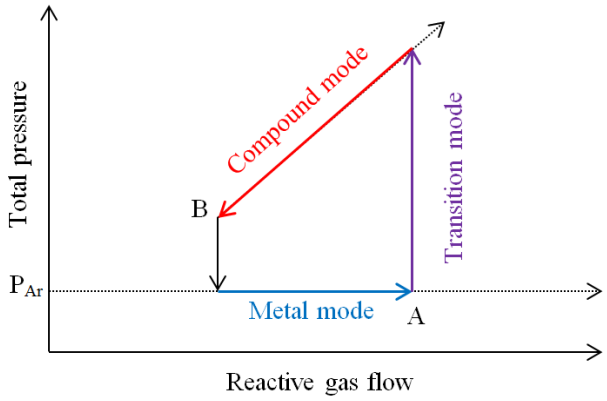

Fig.17: Hysteresis effect, P_{Ar} is partial pressure of working gas Argon in deposition chamber.

Deposition process in this mode makes non-stoichiometric films. Once the flow reaches the certain amount of the reactive gas (A) the total pressure increases. This is caused by insufficient "consuming" of reactive gas in the reactions. After that discharge comes in compound or reactive mode. In this region the reactive gas makes insulating compounds on the target that rapidly reduces sputtering yield, therefore deposition rate is very low in comparison with metal mode (figure 18). Nevertheless deposited films are very often stoichiometric. Decreasing the reactive gas flow the total pressure decreases linearly as well. Reactive gas atoms return to be sufficiently "consumed" in reactions with sputtered atoms, substrate and walls. Insulating compound disappears due to reducing degree of coverage on the target and discharge comes in metallic mode again (B). [24]

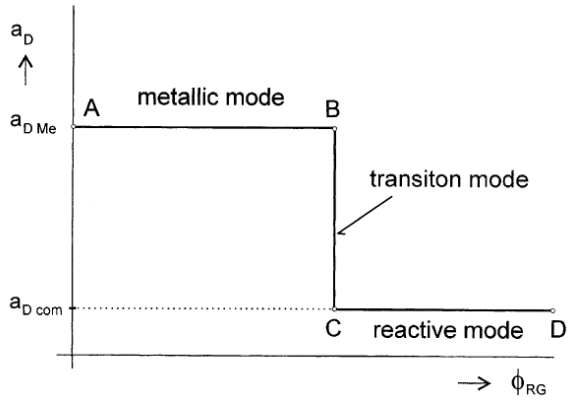

Fig.18: Schematic illustration of deposition rate a_D. Where a_{Dme} is deposition rate of metallic mode, a_{Dcom} composition mode, Φ_{RG} is reactive gas flow. [23]

Transition mode is a non-stable mode. In this region partial pressure of reactive gas is already above zero and the target is not fully covered by insulating compound. Thus sputtering yield and deposition rate are relatively sufficient. Sputtered films can be stoichiometric. Therefore transition mode is very effective in sputtering process. As mentioned above, the sputtering yield of oxides is typically lower than that of metals. Large scale industrial processes require high deposition rates with a stable process. Higher deposition rates can be obtained by sputtering at a suitable point in the transition mode, thereby avoiding a fully poisoned target - using a process control based on dynamic controlling process. [23][24]

There are several ways to control deposition process. Reducing hysteresis effect can be achieved using pumping speed **S** greater than the critical speed $\mathbf{S_c}$, which is defined by following formula.[25]

$$S > S_c = \left(-\frac{\partial^S \Phi_r}{\partial p_r} \right)_{max} \tag{2.5}$$

Another way to control sputtering process is real time control of reactive magnetron deposition by in situ spectroscopic ellipsometry [26]. The process control system operates with an optical monitor for the deposition rate and the film composition in combination with a plasma control setup.

Distinguishing the stoichiometry of sputtered films can be relatively good realized upon optical transparency of the films. Regarding to vanadium oxides coatings and its application becomes this property significant.

2.4.2.2 Arcing in Reactive Sputtering

Arcing is a negative by-product of target poisoning. The build-up of a compound insulating layer on the target results in accumulation of positive ions. After the critical time of charging $\mathbf{t_{cr}}$ (2.6) a breakdown of dialectical layer evokes a discharge with high current and low voltage – arcing.

$$t_{cr} = \varepsilon_0 \varepsilon_r \frac{E}{j} \tag{2.6}$$

When $\boldsymbol{\varepsilon_0}$ is vacuum permittivity, $\boldsymbol{\varepsilon_r}$ is relative permittivity of the insulating layer, **E** is dielectric strength of the layer and **j** is current density at the target. A very thin

insulating layer occurs immediately every time, especially on metal targets. However, as long as it is formed from a couple of monolayers, the charge transport through the insulating layer exists. The reasons are kinetic energy of the impacting ions and tunnelling effect.[27]

One-dimensional scheme for equivalent circuit for the plasma-sheath-insulator-target structure is displayed in figure 19. The insulating layer can be considered as a planar capacitor with one electrode being the target surface. The sheath between insulator surface and plasma is another capacitor. By connecting ion fluid equations, the Poisson equation, and the equivalent circuit equations can be derived an expression for the time-dependent insulator surface potential,

$$\frac{dV_{surf}}{dt} = \frac{dV_{target}}{dt} + \frac{dV_{layer}}{\varepsilon_0 \varepsilon_r}\left(j_i + j_e + j_{disp} + j_{leak}\right). \qquad (2.7)$$

Where $\mathbf{V_{surf}}$ is surface potential, $\mathbf{V_{target}}$ is target potential, $\mathbf{V_{layer}}$ is layer potential and current densities of ions, electrons, displacement (considered only for high frequencies) and leaking through the insulating solid layer, respectively.[27]

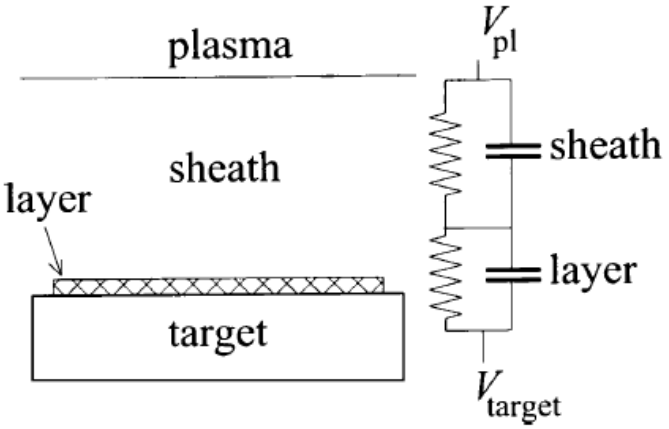

Fig. 19: Schema for 1-dimensional model of sheath and layer between plasma and target, and their equivalent circuit.[27]

While the layer on the target is considerable conducting the leaking current is large and potential of the layer and target is set to a close value. In the next place, when highly insulating layer is formed leaking current is neglected. Then a floating potential is adjusted to balance ion and electron flow from the plasma. Due to higher mobility of electrons than ions, the surface potential will be negative with respect to the plasma potential, of order 10 Volts. That includes that most of the voltage

between target and plasma (several 100 V) is actually dropping in the insulating layer, and the sheath voltage and thickness are reduced accordingly.

Considering unequal sputtering of the target consequently the racetrack area, the insulating layer is mainly formed out of this area. Therefore figure 19 does not correspond to the real situation and two different regions are located. In these zones the sheath accommodates very different voltages. The full cathode falls over the racetrack area and the floating potential over the insulating layer. In contrast to the metal sputter case, the sheath thickness over the racetrack area will be thicker than over the insulating layer as it is shown in figure 20. Transition zone occurs over the tilted edge of the layer. A recent study [27] shows a two – dimensional model for the metal – insulator transition.

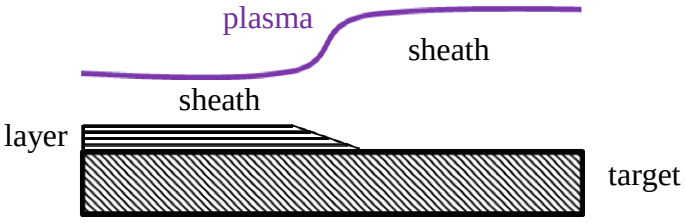

Fig. 20: Schematic of sheath structure at the racetrack edge.

Frequent occurring of arcing in the discharge causes damage and lowers quality of sputtered films therefore an elimination of arcing is the intention. This can be realized by applying radio frequency discharge that very high frequencies (13.56 MHz) avoid forming arcing even in the case of sputtering compound target (insulating materials). As it is mentioned above in formula (2.6) during very high frequencies the displacement current $\mathbf{j_{disp}}$ becomes more significant. Since the positive charge is compensated by incoming electrons from plasma more effectively. Elimination of arcing in HiPIMS power sources is established by process intercepting for a short period. In spite of those precautions arcing can occurs during deposition. Increasing frequency of the power source helps to prevent forming arcing in the discharge. [28]

2.4.2.3 DISAPPEARING ANODE

The other effect that influences reactive sputtering is anode degradation so called the disappearing anode. In sputtering dielectric materials the walls of deposition chamber – anode are covered by dielectric coatings. This insulating layer prevents the anode to operate as ground. In fact, the disappearing anode effect does not have to become significant until the entire anode vanishes. Once certain area is covered, that area ceases to be effective the anode and plasma will shift to find a new lower resistance anode. This shifting of electric field allows plasma to change magnetron deposition patterns. To prevent this ineligible effect dual magnetron deposition was developed and completely eliminates the disappearing anode. Dual magnetron deposition works effectively since it provides a fresh conductive path to each half – cycle. It means that each half – cycle one of two magnetrons is an anode and the second one a cathode. In the next half – cycle their roles swop. This way establishes the closed circuit. Another way how to precede the disappearing anode effect is inserting additional anode from conductive material. However before each deposition mechanical cleaning of the additional anode is necessary. [29]

2.4.3 HIGH POWER IMPULSE MAGNETRON SPUTTERING

In a conventional dc magnetron sputtering (dcMS) the discharge is mainly formed by working gas (Ar) ions. Most of sputtered atoms are neutral, only approx. 1 % atoms are ionized. In respect of thin film density, it is known [30] that an increase in the ion flux greatly reduces intra-columnar as well as inter-columnar porosity, where it is suggested that the incoming ions enhance surface mobility. The increased ion flux on the substrate also improves adhesion and surface roughness.[31] Furthermore the increased ion flux provides a control of the reactivity and lowers the deposition temperature.[32] The presence of high ionized material atoms in plasma attains a great importance for fabrication of electronic applications. Ionized sputtered atoms fill better trenches in semiconductor devices. All these and other advantages of the increased plasma density encourage in increasing the applied power to the target. However, in a conventional dcMS the power density is limited by the thermal load on the target as most of the ion bombarding energy is transformed into heat at the target. These limitations can be moderated by applying high power impulse at the target.

Recently the most utilized technique in ionized physical vapor deposition is high power impulse magnetron sputtering (HiPIMS). The increase in plasma density is simply achieved by applying a high electrical power in pulses with low duty cycle. This mode provides sufficient energy for the ionization of sputtered atoms at the peak and simultaneously keeping average power thus temperature under critical values to prevent overheating. HiPIMS enables to gain higher ionization order of plasma in the zone close to the target. Power density at the peak is in order of kW/cm^2 on the surface target. This leads to electron density between 10^{18} – 10^{19} m^{-3} and ionization of sputtered atoms is around 70 %.[33] HiPIMS discharges typically operates with 500 – 2000 V, current densities 3 – 4 A/cm^2, pulse length 50 – 200 μs, frequency of 50–1000 Hz and low duty cycle in the range of 0.5 – 5 %. The power supply is based on pulse-forming network assemble of single or multiple LC mesh network. Simplified scheme is shown in figure 21.[34]

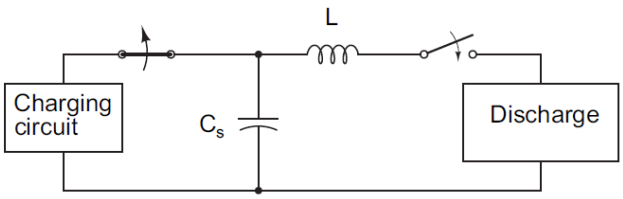

Fig. 21: Simplified scheme of pulse generator.[34]

2.4.3.1 Delayed Current Onset

In paper [35] by Kouznetsov et al. a significant time delay between the current and voltage onset in time trace was noted. A Cu cathode was used and Argon sputtering gas was maintained at 0.065 Pa. As figure 22 shows, the time delay of magnetron discharge ignition was 50 μs, which is characterized by a drop of voltage in hundreds of volts. This time delay that can be always seen in HiPIMS processes is examined in [36] in order to get a correspondence with theoretical considerations for discharge breakdown.

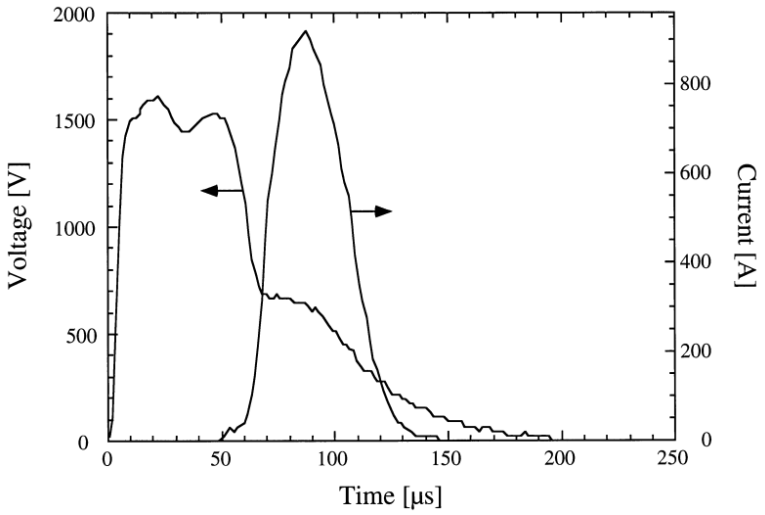

Fig. 22: Typical current and voltage time trace for HiPIMS.[35]

Following the concepts of breakdown, the time delay of current onset is composed of the statistical time lag $\mathbf{t_s}$ and the formative time lag $\mathbf{t_f}$. The statistical time lag is given by some time delay of an origin of initial electrons in an electric field between the electrodes. The formative time lag represents a time delay for a creation of plasma discharge using the initial electrons. Hence the total time delay $\mathbf{t_d}$ is written as

$$t_d = t_s + t_f. \tag{2.8}$$

Since pulsed systems generally operate with a large overvoltage in order to obtain a discharge and considering the case when initial electrons are present (left over from previous pulse – discharge) subsequently $\mathbf{t_s} << \mathbf{t_f}$. Formative lag time can be approximated by

$$t_f \approx \frac{a}{V - V_0} e^{\frac{b}{V_0}}, \tag{2.9}$$

where $\mathbf{V_0}$ is the static breakdown voltage, **V** is the applied voltage, $\mathbf{a} = \mathbf{A_p}$, and $\mathbf{b} = \mathbf{B_{pd}}$, where **A** and **B** are constants determined experimentally and depend on the gas type. In conclusion this delay depends on the gas pressure [37], target material – secondary electrons emission is important (figure 23) and applied voltage (figure 24).[36]

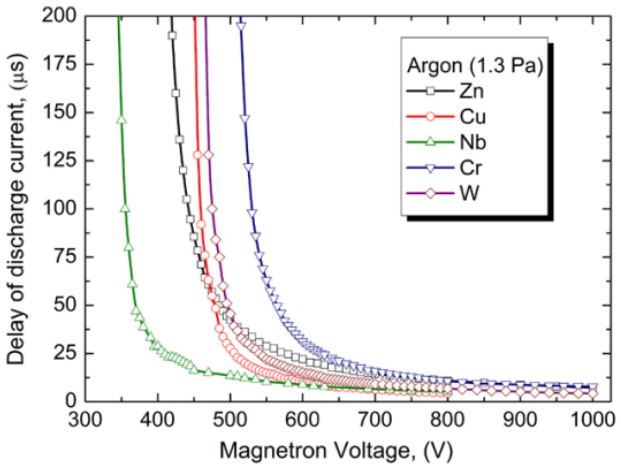

Fig. 23: Delay of the current onset as a function of the applied voltage for different target materials.[36]

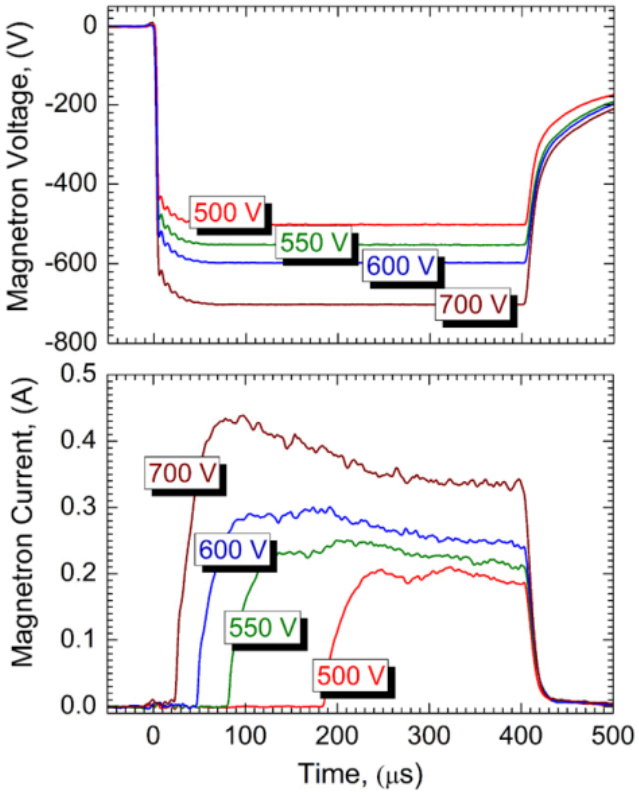

Fig. 24: Illustration of the current delay, with the applied voltage as a parameters; applied voltage (top) and discharge current of a magnetron discharge (bottom); Cu target, Ar 1.3 Pa, 100 pulses per second.[36]

2.4.3.2 Gas Rarefaction

The flux of sputtered atoms and reflected ions, which became neutral atoms over again, has a significant influence on the working gas in front of the target. Most of the sputtered atoms are slowed down by collisions with the working gas, particularly when the pressure of the working gas is relatively high. The atoms of the working gas (Ar) are locally displaced further from the target towards to the substrate. This effect includes gas heating and expansion, it is known as gas rarefaction. The rarefaction of the working gas is even more pronounced at higher powers, the back attracted excited target ions and especially the doubly ionized target atoms, are able to partially substitute the role of Ar ions in the generation of the secondary electrons. Target materials of higher sputter yield have greater effects, and of course the mass ratio of sputtered atoms and gas atoms has a great influence on how much energy and momentum is transferred from the sputter flux

to the gas. Sputtered atoms have typically several eV of kinetic energy, following the Sigmund-Thompson theory, the energy distribution function is approximated by

$$f_{S-T}(E) \propto \frac{E}{(E + E_{SB})^3}\,, \tag{2.10}$$

where the surface binding energy $\mathbf{E_{SB}}$ is an significant material parameter. The surface binding energy together with sputtering yield indicates an important role of target material in the phenomena gas rarefaction (sputter wind). [39]

In time-current pulse characteristics the process of the gas rarefaction can be observed closely. The influence of gas pressure on the gas rarefaction is well displayed in figure 25. The magnitude of the initial peak and the following decay is more pronounced when the working gas pressure is high. The origin of the initial peak is explained by increasing discharge current that is composed of the ion current to the target $\mathbf{I_i}$ and the current of secondary electrons $\mathbf{I_{SE}}$ from it,

$$I = I_i + I_{SE} = I_i(1 + \gamma_{SE}). \tag{2.11}$$

Where $\boldsymbol{\gamma_{SE}}$ is the yield of secondary electrons. As ionization of the working gas becomes strong, the sputtered atoms from the target collide with the gas atoms. This leads to a compression of the gas, thereby providing transient conditions for the generation of an even stronger ion current to the target.[39][22]

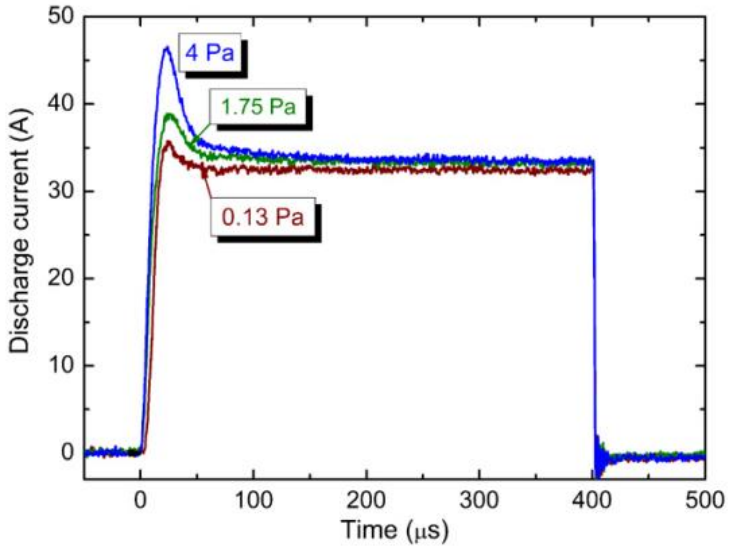

Fig.25: Time - discharge current characteristic. For copper target, the applied voltage was 1000 V, which was constant during the 400 μs pulse.[39]

Paper [38] discusses time - current behavior in typical HiPIMS pulses during sputtering niobium target. Investigated characteristics of the discharge current and voltage are shown in figure 26. It is shown that the HiPIMS power supply applies a maximum $\mathbf{U_C}$ instantly at the beginning of the pulse, followed by a current rise. The resulting high instantaneous current density decreases the cathode sheath thickness, which in turn increases the probability of arcing that can limit the deposition process. HiPIMS discharge breakdown is characterized by a detection of the emission peak of Ar^0 excited by the energetic electrons. Onset of the target sputtering is denoted by a rise of Ar^+ and of both neutral and ionized Nb emissions. A large number of sputtered metal atoms then enter in collision with the working gas and cause its localized heating and rarefaction.

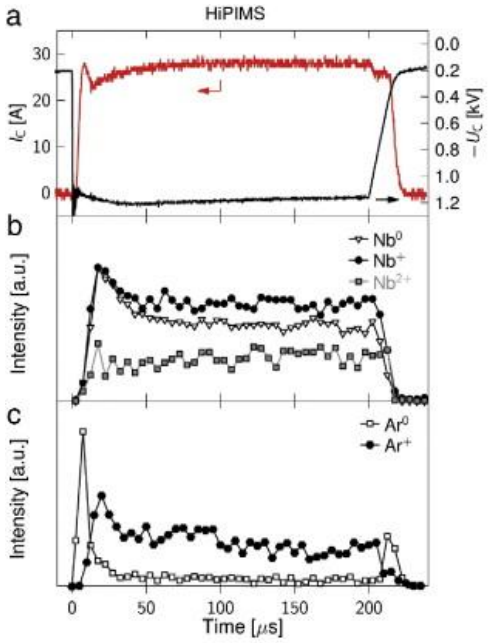

Fig. 26: Time evolution of the discharge current I_C and the cathode voltage U_C (a), and of the optical emission intensities originating from the excited metal species (b) and working gas species (c), recorded during a 200 μs. The discharge was operated in Ar at p = 1 Pa and at P = 300 W. The acquisition time for different monitored species was not normalized.[38]

When the sputtered metal enters into the plasma zone, it results in significant electron cooling due to inelastic electron–metal collisions. The latter effect is the principal origin of the drop in the emission intensities of Ar^+ and also of the metallic emission lines, following their peak at **t** = 20 μs. The rest of the pulse, **t** > 75 μs, the emission intensities of all Nb lines are approximately steady, similar to the $\mathbf{U_C}$ and $\mathbf{I_C}$ values.[38]

2.4.3.3 SELF-SPUTTERING EFFECT

Origination of ionized sputtering is dated in 1970s in Japan. In 1980 authors of [40] came up with self-sputtering effect of high ionized atoms as a consequence of high ionization in HiPIMS. A part of ionized material atoms return to the target and participate in sputtering of atoms at the target. The principle of self-sputtering is displayed in figure 27. Self-sputtering is a significant effect during sputtering high sputter yield materials like copper, silver, zinc and niobium. This mode helps to sustain plasma discharge thus argon or other inert gases are only used to start up the deposition process. Avoiding working gas in deposition process enables forming films without incorporating atoms of the working gas and decreasing working pressure therefore increasing transferred energy onto a substrate. The condition for sustained self-sputtering and runaway mode reads

$$\pi \equiv \alpha\beta\gamma_{ss} \geq 1 \tag{2.12}$$

where $\boldsymbol{\alpha}$ is the ionization probability, $\boldsymbol{\beta}$ is the probability that a sputtered and ionized atom will return to the target and $\boldsymbol{\gamma_{ss}}$ is self-sputter yield. Runaway mode can be understood in this way: the more atoms are sputtered the more can be ionized; and the more ions return to the target the more atoms can be sputtered from the target. In figure 28 current-voltage-time characteristics for a cooper target are shown. When the applied voltage is below 535 V, current decreases after some time, which is caused by sputter wind effect. However, higher applied voltage supplies enough energy to evoke self-sputtering that leads to compensation of sputter-wind effect.[41] Runaway mode can amplify itself until some limitations that are set by the power supply. If the power supply is able to deliver enough high current to the discharge other physical limitations will appear. One can see that increasing self-sputtering effect decreases flux of sputtered atoms to the substrate. When $\boldsymbol{\alpha} < 1$ and $\boldsymbol{\beta} < 1$, the condition $\boldsymbol{\gamma_{ss}} > 1$ is necessary however not sufficient for sustained self-sputtering. Temporary runaway mode happens when $\boldsymbol{\pi} > 1$. This mode can be observed in figure 28 as the inclined edge in current-voltage-time characteristics. Once the current settles at a high level steady-state $\boldsymbol{\pi} = 1$ is hold. [22]

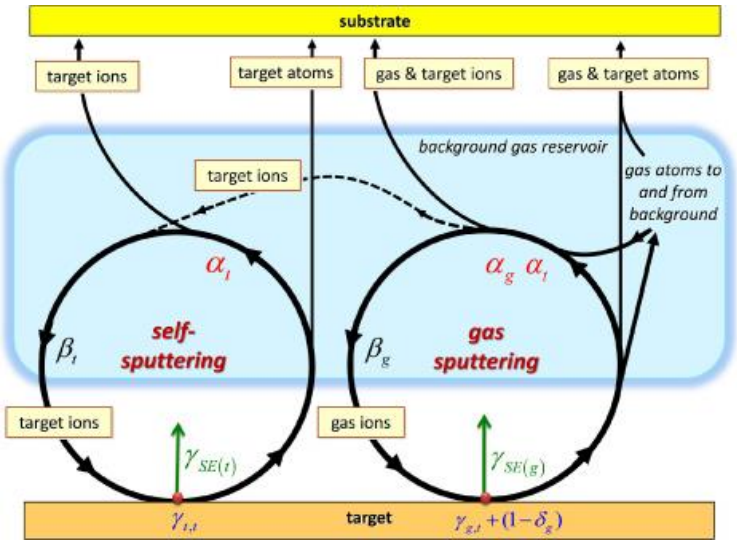

Fig. 27: The principal of self-sputtering effect.[42]

The ionization probability is affected by secondary electron energy. Secondary electrons gain their energy transiting the sheath and participate in ionization process. Since very low ionization energy of metal atoms compared to argon atoms, secondary electron emission is considerably reduced in self-sputtering mode. This results in reduction of secondary electron flux and decreasing ionization process. Contrary to the reduction of ionization process operate high ionized metal atoms and interaction of ultra-violet photons with the target. [43]

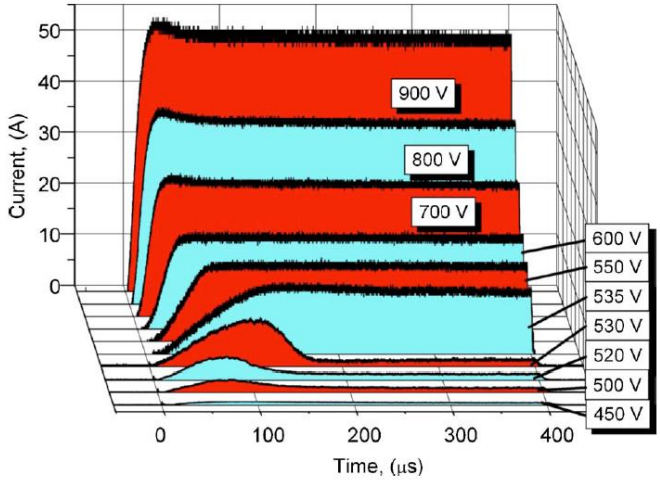

Fig. 28: Current pulse shapes at different constant voltage for a copper magnetron discharge in argon at 1.8 Pa. [41]

CHAPTER 3: AIMS OF THE THESIS

1. Do research about present problematic and deepen knowledge of high power reactive magnetron sputtering of vanadium oxides.

2. Familiarize with the experimental system and techniques for preparation and analysis of thin films at the Department of Physics.

3. Accomplish preparation of chosen series of thin films and its characterization under supervision.

4. Find a relation among parameters of magnetron discharge, deposition characteristics and nature of sputtered films.

CHAPTER 4: EXPERIMENTAL DETAILS

4.1 POWER SUPPLY

Used power supply belongs in the TruPlasma Highpulse Series 4000 power supplies designed by TRUMPF Hüttinger Company. It is especially designed to generate high density plasmas. Detailed specification of the TruPlasma Highpulse 4002 generator is contained in table 4.1. The power set consists of three modules: the DC charging unit, the high impulse generator unit and Low Power Adapter unit. The generator is also equipped by an arc detection feature. The serial semiconductor switch is immediately turned off if the output pulse-current exceeds a specified value. By reason of controlling the parameters of pulse the power supply was connected to the control unit via analogues and digital inputs and outputs.

Table 4.1: The TruPlasma Highpulse 4002 – Pulse Unit	
Output voltage	2000 V
Output current	1000 A
Total mean power	10 000 W
Frequency	2 – 500 Hz
Pulse duration	1 – 200 μs
Capacitance	125 μF

4.2 DEPOSITION SYSTEM

Deposition chamber is pumped onto primary pressure below 1×10^{-4} Pa through serial integration of dry mechanical pump Adixen ACP 28 based on multi-stage roots technology by Alcatel Vacuum Technology and a turbomolecular pump HiPace 1200 by Pfeiffer Vacuum. The mechanical pump supports the pumping in order to achieve the effective pumping speed of the turbomolecular pump 1200 l/s, which is usually achieved in tens of Pascal. The peak pumping speed of the mechanical pump was 7.5 l/s. The following block diagram in figure 29 shows the vacuum system. Samples are always placed in a load-locked chamber (2) and transferred to the deposition chamber (1). The load-locked chamber provides a possibility to avoid aeration of the deposition chamber while inserting samples. Pumping of the load-lock chamber is provided by turbomolecular pump HiPace 80 by Pfeiffer Vacuum, its pumping speed

is 67 l/s and this pump is supported by diaphragm pump MVP 070-3 (0.9 l/s) also by Pfeiffer Vacuum.

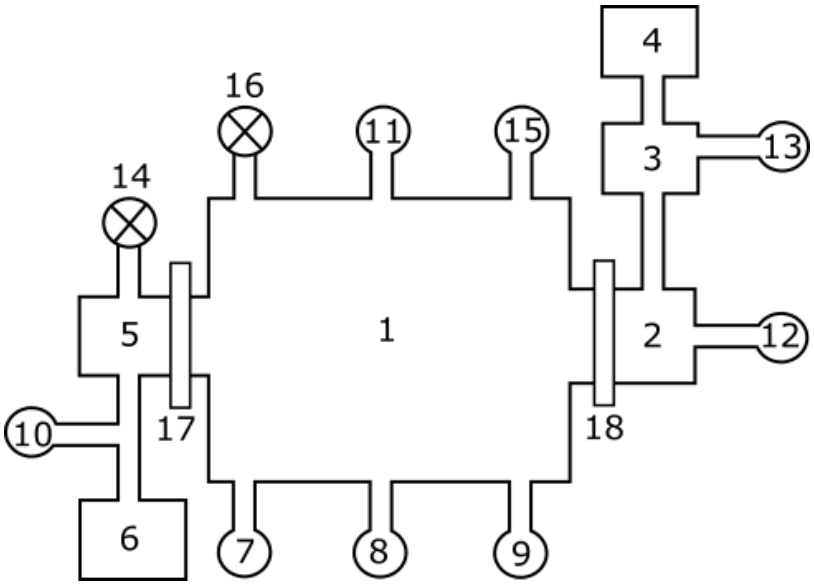

Fig.29: Pumping system; (1) deposition chamber, (2) load-locked chamber, (3) turbomolecular pump HiPace 80, (4) diaphragm pump, (5) turbomolecular pump HiPace 1200, (6) roots pump, (7) capacitance manometer BARATRON, (8) Pirani gauge, (9) Bayard – Alpert ionization gauge, (11) working gas inlet, (10)(12) vacuum pressure transducer 974 QuadMag, (13) gas - N_2 inlet,(15) reactive gas inlet, (14)(16) air valve, (17) (18) gate valve.

Dimensions of the stainless cylindrical deposition chamber are 558 mm in diameter and 419 mm in length. The chamber is interconnected with load-locked chamber via a gate valve (18) as it is shown in figure 29. Total pressure in the deposition chamber is measured by capacitance manometer BARATON (7) in range of pressure 0 – 100 mTorr. It measures real absolute pressure (defined as force/unit area). This means that the measurement is insensitive to the type of gas being measured. Except deposition process the pressure is measured with The 275 Convectron Pirani Gauge by MKS Instruments (8) and Bayard – Alpert ionization gauge by Granville-Phillips (9). The Pirani gauge is a thermocouple measuring known gas in a range of 10^{-2} – 10^{5} Pa. The Bayard – Alpert gauge ionizes the gas molecules within the gauge volume, collects those ions on a thin ion collector wire, and measures the resulting current to the ion collector to determine the number of molecules present and indicates a pressure based on that measurement. The operation range of B-A gauge is 10^{-8} – 10^{0} Pa. Pressure in the load-locked chamber and in the pipe between the turbo and the roots pump is measured by The 974 QuadMag™ vacuum

transducer by MKS Instruments (12) and (10), respectively. The vacuum transducer offers a measuring range from 10^{-5} to 10^{5} Pa and is based on measurement of thermal conductivity, mechanical deflection of a silicon membrane and cold cathode ionization current. Gas input of the deposition chamber is realized by a feed through (11) for working gas and another feed through (15) for reactive gas. The gas flow is controlled by two Mass-flow controllers M100B by MKS Instruments. Working gas (Ar) is controlled by a mass-flow controller in range 0 – 100 sccm and oxygen in 0 – 20 sccm. All the mass-flow controllers are connected to a control unit, which provides a possibility to regulate reactive gas flow as well as the deposition process. The control unit (PLC system) collects all connected signals during the whole deposition with a sampling rate 10 ms. In order to keep invariable pressure during the deposition process the gate valve (17) is adjusted to a certain position to allow appropriate pumping of gas.

Detailed scheme of the deposition chamber is illustrated in figure 30. Reactive gas (O_2) flows into the chamber via a korund tube 2 mm in diameter with two holes 1 mm in diameter. The adjustment of reactive gas inlet is to-substrate as shown in figure 30. The tube was placed in 20 mm from the target. In distance 150 mm from the target is situated a rotating substrate holder with four samples, which can be shade with a shutter to prevent an unwanted deposition onto the substrates. The holder is equipped with a substrate heater and air-cooling. Glass and Si (100) were used as substrates for the samples.

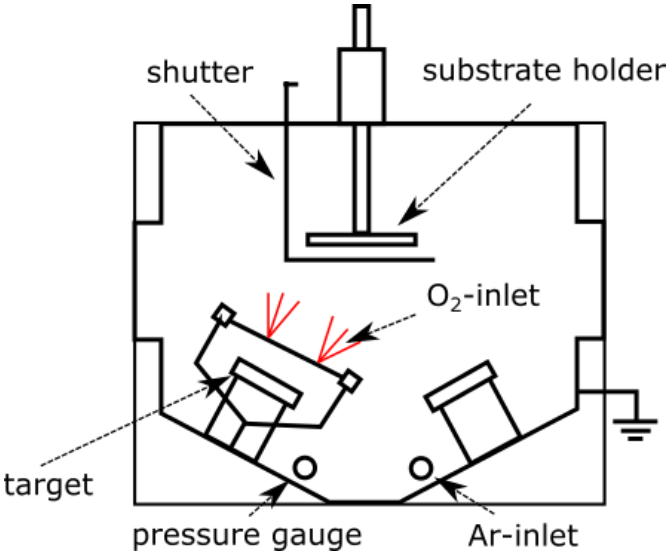

Fig.30: Illustration of deposition chamber.

Another part of deposition chamber is unbalanced magnetron, which is electrically insulated from the deposition chamber. The magnetic field of the magnetron is formed by permanent concentric circular magnets made of Nd-Fe-B (a neodymium magnet). Magnetron is equipped with vanadium target (99.999%) of diameter 50 mm and 6.3 mm thick, which is fasten with a glazing ringlet. Due to conversion of ion kinetic energy to heat, which is transferred to the magnets, it is necessary to water – cool magnetron. Otherwise if the temperature of magnetron exceeded Currier temperature $\mathbf{T_c}$ = 347 °C ($Nd_2Fe_{14}B$) magnets would lost its magnetic features.

4.3 CONTROL SYSTEM

In order to control stoichiometry of sputtered films a control system was utilized in the deposition process. The control system was developed at the Department of Physics at Faculty of Applied Sciences in purpose to accomplish reactive deposition of oxides specially ZrO_2, Ta_2O_5 and TaON. The control system allows achieving higher deposition rates and stabilizes the deposition process. The principle of controlling algorithm is explained in figure 31.

First of all, the control system can be set to test sensitivity to a unit-pulse flow of reactive gas. Monitoring parameter of the system is current and total pressure in deposition chamber. The current is defined as an average current in a period of pulse of the voltage power supply. Sensitivity of the monitoring quantitates may vary depending on target material. Secondary electron emissivity plays an important role in matter of the sensitivity, since it is affected by forming of compound on the target. More sensitive quantitates (average current or pressure) becomes a control parameter. Behaviour of quantitates is necessary to be observed at the beginning and the end of activation of reactive gas flow. [24]

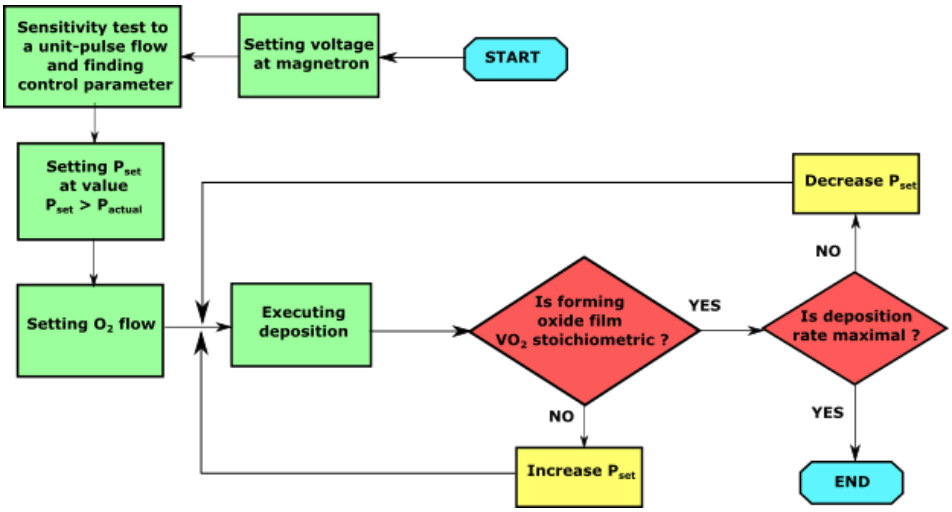

Fig. 31: Flowchart illustrating fundamental principle of finding optimal value of I_{set}.[24]

As shown in figure 31 fundamental principle operates with controlling the reactive gas flow based on condition (4.1) where $\mathbf{I_{actual}}$ is a measuring value of control parameter, $\mathbf{I_{set}}$ is a control parameter of control algorithm (user command), $\mathbf{\Phi_{reactive}}$ is reactive gas flow and **X** is a value of the gas flow set by user. Owing to the condition reactive gas starts pulsing in a variant period between two following pulses. After several calibration depositions an optimal value of control parameter is found with respect to required film properties. Nevertheless deposition conditions (total pressure, pulse length, frequency, voltage etc.) must be unchangeable. Basically the controlled process allows sputtering stoichiometric films in transitions mode.[24]

$$I_{actual} \geq I_{set} \Longrightarrow \Phi_{reactive} = 0 \wedge I_{actual} < I_{set} \Longrightarrow \Phi_{reactive} = X \qquad (4.1)$$

4.4 FILM PREPARATION

All presented samples in this thesis were prepared under following deposition conditions, which are described in this chapter. All substrates were placed in acetone bath and cleaned by ultrasonic waves for 10 min. After cleaning the substrates were fasten to a circular substrate holder. Distance between the substrate holder and target was 150 mm. Before deposition a substrate etching process were running for 2 min. The operation RF power of the etching process was 30 W.

General characteristics the deposition process:

- Deposition chamber was pumped down < 10^{-4} Pa
- Working pressure 1.0 Pa
- Working gas (Ar) flow rate was 60 sccm
- Reactive gas (O_2) flow rate was 0 or 2 sccm

4.5 INSTRUMENTS OF ANALYSES

4.5.1 MEASUREMENT OF FILM THICKNESS AND DEPOSITION RATE

Film thickness was primarily evaluated at Profilometer Dektak 8 Stylus by Veeco Company. The measurements were performed on a "floating" table, which minimizes the effect of floor vibrations. The measurement is mechanical: a diamond tip (under a defined load) follows the sample profile along a chosen trajectory. The tip is connected to linear variable differential transformer unit which converts its vertical position of deflection to a corresponding electrical signal. Software that controls the measurement provides an evaluation and possibility to set parameters such as applied load, measured trajectory and motion of the table with substrate and so on. Deposition rate was determined as a ratio of film thickness and time of deposition process. Conclusive values of thickness were specified by ellipsometry at apparatus VASE by J.A.Woollam, Co. Inc. The measurement was accomplished by doc. Ing. J. Houška, Ph.D.

4.5.2 OPTICAL CHARACTERIZATION – ELLIPSOMETRY

Ellipsometry is a very sensitive optical characterization technique. It measures the change of (generally elliptical) polarization of light after its reflection from a sample as shown in figure 32. Measurements were accomplished at an ex-situ

spectroscopic ellipsometer VASE by J.A.Woollam. The wavelength range is 250 to 2500 nm. The instrument includes automatic goniometer (angle range 20 to 90° in the case of reflection and -45 to 90° in the case of transmission), microspot optics (0.1 mm measurement spot) and INSTEC cell which allows cooling (liquid nitrogen) and heating (up to 600 °C) of a sample.

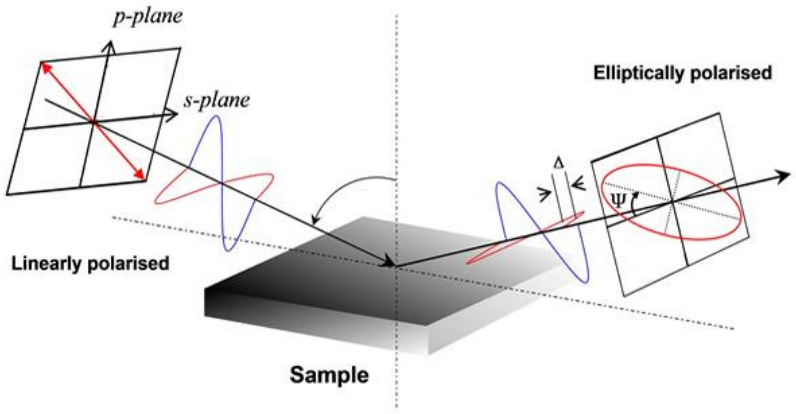

Figure 32: The principle of elliptical polarization in ellipsometry.[44]

The change of polarization of light is presented with two parameters describing an ellipse formed by the endpoint of the electric–field intensity vector. These parameters are ellipsometric angles **Ψ** and Δ. First ellipsometric angle **Ψ** is defined as a ratio of Fresnel's coefficients and $tan\,(\boldsymbol{\Psi})$ stands for intensity difference. The second ellipsometric angle Δ is a change of phase shift of perpendicular polarized waves. The interaction of light and interface is expressed by non-dimensional complex relative permittivity (4.2) or a complex refractive index (4.3). Its real and imaginary parts are denoted as:

$$\varepsilon_r(\omega) = \varepsilon_1(\omega) + i\varepsilon_2(\omega) \tag{4.2}$$

$$n(\omega) = n_1(\omega) + ik(\omega) \tag{4.3}$$

Where, the real relative permittivity $\boldsymbol{\varepsilon_1}$ is known as static relative permittivity for frequencies close to zero. The complex part $\boldsymbol{\varepsilon_2}$ indicates dielectric loss at high frequencies. The real part $\mathbf{n_1}$ is the refractive index and indicates the phase velocity, while the imaginary part **κ** is called the "extinction coefficient" and indicates the amount of attenuation loss when the electromagnetic wave propagates through the material.[44]

Ellipsometric measurements provide valuable information concerning change in polarization that can be utilized for calculation of optical parameters such as refractive index **n** and extinction coefficient **k**. Furthermore, transmittance can be calculated from these optical parameters.

In the case of thermochromic materials changes in polarization of outgoing rays were investigated in dependence on the film temperature. Illustration of that kind of measurement is in figure 33. While the film temperature was increasing and decreasing an ellipsometric angle **Ψ** was changing from Ψ_{min} as shown in figure 33. Hysteresis behaviour of the material can be obtained from collected data. Cycled temperature changes can indicate thermochromic characteristics as well.

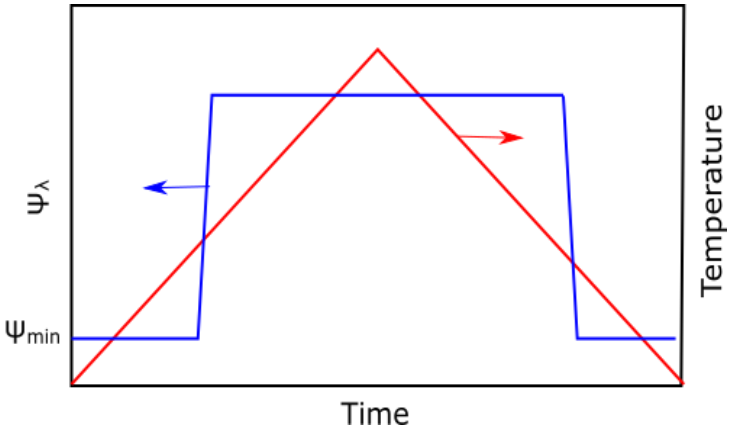

Fig. 33: Schematic principle of ellipsometric measurements for theromchromic materials.

4.5.3 Optical Characterization – Raman Spectroscopy

Raman spectroscopy is a molecular spectroscopy which measures a frequency shift of inelastically scattered light from material. It allows for interaction of a laser beam with vibrational – phonon states of molecules. Comaparing Raman spectroscopy to the infrared spectroscopy, both register vibrational frequencies of bonds presented in material. However Raman spectroscopy registers vibrational modes leading to a polarizability change. As a result, Raman spectroscopy provides an invaluable analytical tool for molecular finger printing as well as monitoring changes in molecular bond structure. [45]

Measurements were accomplished by doc. Ing. J. Houška, Ph.D. at Raman spectroscope LABRAM by Horiba Jobin Yvon. The measurements can be performed with three different lasers (incident wavelengths): 325, 532 and 785 nm.

The instrument is equipped with a confocal microscope with a motorized sample holder.

4.5.4 Structural Analysis

Phase composition of deposited films was analysed by X-ray diffraction (Bragg – Brentan arrangement) at multifunctional powder X-ray diffractometer X'Pert Pro MPD by PANalytical. The diffractometer is equipped with Cu – X-ray tube (40 kV, 40 mA) and wavelength of x-ray beam is 0.154187 nm. Diffracted rays were detected by a semiconductor detector X'Celerator that is provided by a nickel filter to remove Cu-Kβ rays from a diffractogram. The measurements were accomplished by Ing. R. Čerstvý.

Fundamental principle is based on Bragg's Law and a scheme of X-ray diffractometer is displayed in figure 34. Emitted X-ray beams come out of an X-ray tube (source) and collide with a crystalline sample. X-rays are partially scattered by atoms when they strike the surface of a crystal. If beams diffracted by two different layers are in phase, constructive interference occurs and the diffraction pattern shows a peak. The diffraction peaks only occur if

$$2dsin(\theta) = n\lambda \tag{4.2}$$

where **θ** is the angle of incidence of the X-ray, **n** is an integer, **λ** is the wavelength, and **d** is the spacing between atom layers. When the wavelength of x-rays and the angle of incidence are known, it is possible to calculate the inter-layer distance and determine the crystal structure. [46]

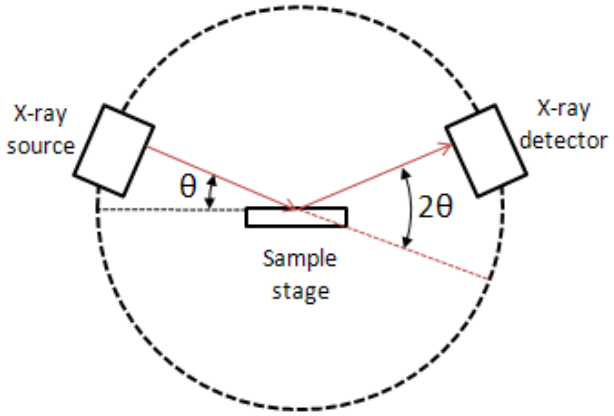

Fig. 34: Scheme of X-ray difractometer.[46]

CHAPTER 5: RESULTS

This chapter presents the results of sputtered vanadium oxide films. There were twelve samples prepared in total. First part of the presented chapter demonstrates discharge and deposition characteristics (voltage and current density characteristics at the target, target power density etc.). The second part examines optical properties (refractive index, extinction coefficient) of prepared films and its structure.

5.1 DEPOSITION PARAMETERS

Tab 5.1: Deposition parameters of sputtering process	
Total pressure	1.0 Pa
Working gas	argon
Reactive gas	oxygen
Average target power density	12.4 – 14.0 W/cm^2
Pulse repetition	125, 200, 250 Hz
Pulse duration	40, 50, 80 μs
Duty cycle	0.01 (1 %)
Pulse voltage	595 – 610 V
Target material	Vanadium (99.999%)
Target – substrate distance	150 mm
Substrate material	Si (100), glass
Bias Substrate	floating potential
Substrate temperature	ambient temp. or 400 °C

Average target power density $\langle S_d \rangle$ belongs to the most significant parameters of deposition process. It is given

$$< S_d > = \frac{1}{t_e - t_s} \int_{t_s}^{t_e} U_d(t) \times J_t(t) dt \qquad (5.1)$$

where t_s and t_e is time of start and end of the deposition process, respectively. $U_d(t)$ is instant magnetron voltage, $J_t(t)$ is instant current density at the target, which is defined as $J_t(t) = I_d(t)/S_{target}$, when $I_d(t)$ is instant current at the target and target area S_{target} = 19.63 cm^2. Applying the same integral formula (5.1) the average flow rate $\langle \Phi_{ox} \rangle$ can be calculated. Average target density at a pulse S_{da} is denoted as:

$$S_{da} = \frac{1}{t_1} \times \int_0^{t_1} U_d(t) \times J_t(t) dt \tag{5.2}$$

where $\mathbf{t_1}$ is voltage pulse length. Time variable value of average current at the target $\mathbf{\bar{I}_d}$ in a period of power supply **T** is formulated in (5.3) when **T = 1/f**, **f** is repetition frequency of the power supply.

$$\bar{I_d} = \frac{1}{T} \times \int_0^{T} I_d(t) dt \tag{5.3}$$

5.2 Process and Discharge Parameters

Process parameters are summarized in table 5.2. There are samples divided into three groups according to the voltage pulse length 40, 50 and 80 μs. In order to keep duty cycle = 1 % the pulse frequency was 250, 200 and 125 Hz in respect of the pulse length. A half of the samples was heated up to 400 °C during the whole deposition process for each voltage pulse length. The second half was prepared at the ambient temperature. As shown in table 5.2 the average target power density $\mathbf{<S_d>}$ was almost constant for all samples, the average flow rate of oxygen as well. Another important parameter is deposition time, which influences film thickness. In respect of the film thickness, two types of films were prepared. There is "thin" and "thick" film for every temperature in each group of the voltage pulse length.

Tab 5.2: Process parameters

Frequency f (Hz)	Pulse length t_1 (μs)	Heating T (°C)	$<S_d>$ (W/cm^2)	S_{da} (W/cm^2)	$<\phi_{ox}>$ (sccm)	Deposition time t (s)
125	80	< 40	14.0	940 - 1575	1.21	1350
		400	-	-	-	1350
		< 40	13.9	905 - 1580	1.26	2700
		400	13.9	915 - 1645	1.24	2700
200	50	< 40	13.1	840 - 1440	1.21	1500
		400	13.0	930 - 1605	1.23	1500
		< 40	13.0	945 - 1520	1.22	3000
		400	13.0	865 - 1300	1.22	3000
250	40	< 40	12.4	925 - 1375	1.28	1600
		400	13.2	970 - 1430	1.25	1600
		< 40	13.2	785 - 1425	1.22	3200
		400	13.0	910 - 1340	1.25	3200

Evolutions of instant current at the target $\mathbf{I_t}$, partial oxygen pressure $\mathbf{p_{ox}}$ and oxygen flow rate $\boldsymbol{\phi_{ox}}$ are illustrated in figure 35. These evolutions belong to a sputtering process with the voltage pulse length $\mathbf{t_1}$ = 80 μs, average oxygen flow rate $\langle\boldsymbol{\phi_{ox}}\rangle$ = 1.24 sccm, average target power density $\langle\mathbf{S_d}\rangle$ = 13.9 W/cm^2 and deposition time **t** = 2700 s. The control parameter of the control system is instant current at the target $\mathbf{I_t}$. Current threshold is set at certain value to avoid target poisoning thus arcing. If the value of instant current $\mathbf{I_t}$ is higher than current threshold $\mathbf{I_{set}}$, an oxygen inlet is off, which reduces forming of a vanadium oxide layer on the target. This results in a current decreasing as shown in figure 35. When the instant current drops below the current threshold, the oxygen inlet is on and the entire process is repeated.

Evolutions of instant current at the target $\mathbf{I_t}$, partial oxygen pressure $\mathbf{p_{ox}}$ and an oxygen flow rate $\boldsymbol{\phi_{ox}}$ for other process parametres described in table 5.2 show equivalent forms and behaviour as illustrated in figure 35.

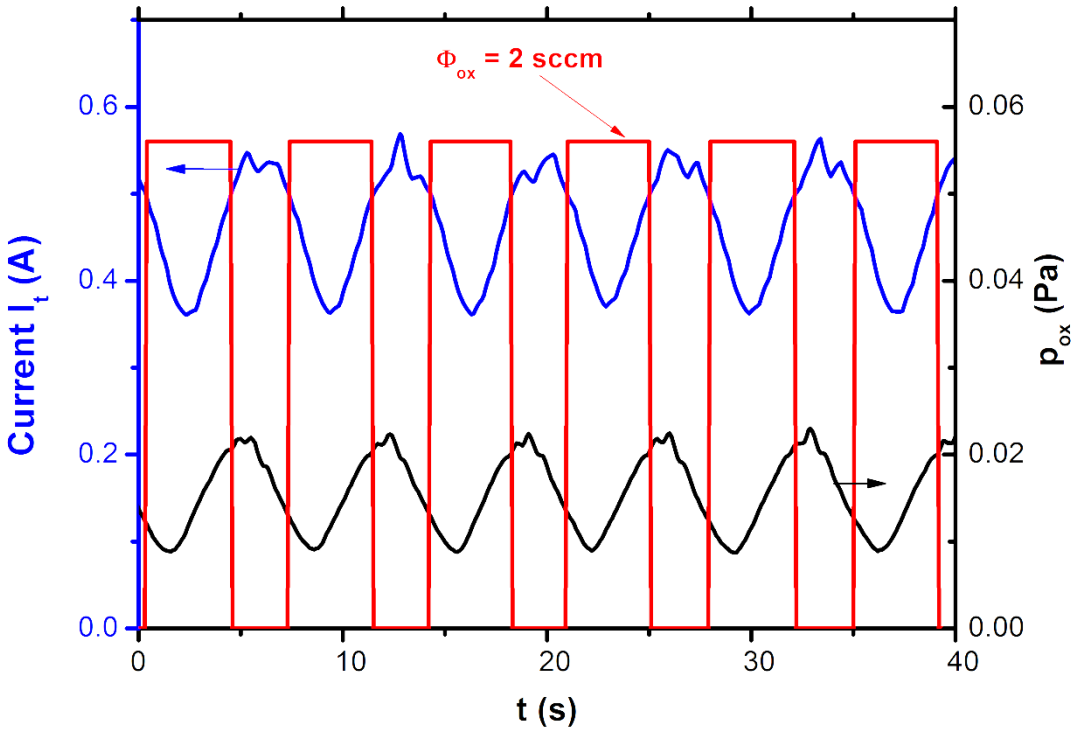

Fig. 35: Evolutions of instant current I_t at the target (control parameter), partial pressure of oxygen p_{ox} and oxygen flow rate ϕ_{ox}. Pulse length t_1 = 80 μs, average oxygen flow rate $\langle\phi_{ox}\rangle$ = 1.24 sccm, average target power density $\langle S_d \rangle$ = 13.9 W/cm^2 and deposition time t = 2700 s.

Following figure 36 displays current density at the target $\mathbf{J_t}$ and voltage wave forms. The wave forms show behaviour of maximal (red curve) and minimal (blue curve) current density in a pulse as well as behaviour of maximal and minimal voltage. The length of the pulse is 80 μs. Illustrated oscillation of voltage and current density is given by pulsing of instant current $\mathbf{I_t}$ in figure 35. For maximal values of voltage and current density $\mathbf{J_t}$ is average target density at a pulse $\mathbf{S_{da}}$ = 1645 W/cm^2 and for minimal values is S_{da} = 915 W/cm^2. One can notice that the minimal voltage does not decrease to zero as the maximal does. Explanation of that difference rests in insufficient discharging of the power supply capacitors due to the lower current.

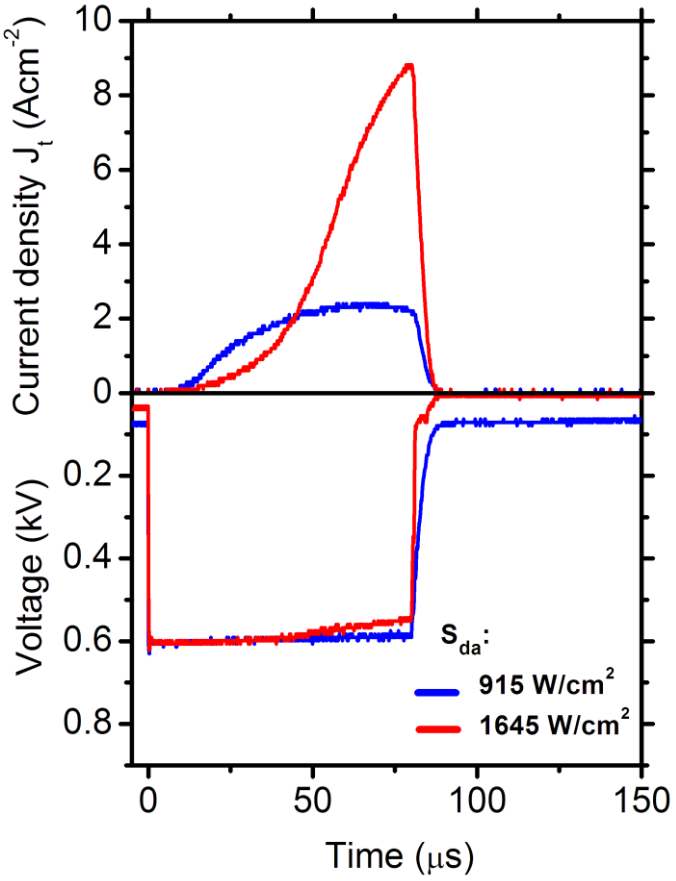

Fig. 36: Current density J_t and voltage wave forms. The red wave forms correspond to maximal value of control parameter I_t and the blue wave forms correspond to minimal value I_t. Average target density at a pulse S_{da} = 1645 W/cm^2 for maximal values of voltage and current density. S_{da} = 915 W/cm^2 for minimal values of voltage and current density. Pulse length t_1 = 80 μs.

5.3 STRUCTURE CHARACTERIZATION OF THE FILMS

This section describes structural properties analysed by XRD and Raman analysis. Subsequently optical characterization of the samples such as refraction index **n**, extinction coefficient **k** and change ellipsometric angle **ΔΨ** are investigated.

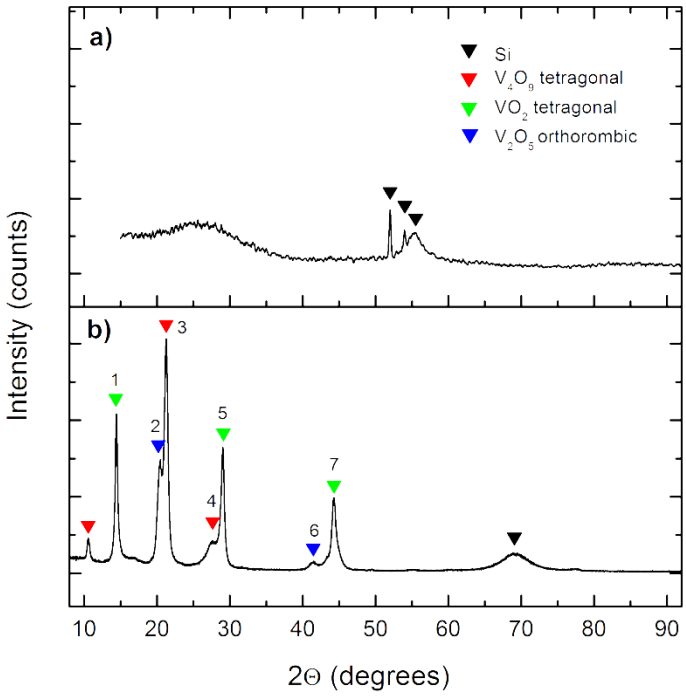

Fig. 37: XRD patterns of prepared thin films at pulse length t_1 = 50 μs, average target power density $<S_d>$ = 13.0 W/cm^2, deposition time t = 3000 s. and (a) no substrate heating, (b) substrate heating T = 400 °C. Crystallite orientation: 1 – (110), 2 – (001), 3 – (200), 4 – (103), 5 – (220), 6 – (002), 7 – (330).

Obtained XRD patterns of all sputtered thin films show three structural natures. Two structural characterizations of thin films are presented in figure 37. Pattern (a) shows an amorphous structure due to an absence of any peaks belonging to a crystalline structure. It was sputtered at the voltage pulse length $\mathbf{t}_1$ = 50 μs, no substrate heating, average target power density $\mathbf{<S_d>}$ = 13.0 W/cm^2 and deposition time **t** = 3000 s. It was determined that significant process parameter affecting structure is a substrate heating since all samples prepared without the substrate heating exhibit amorphous structure. Peaks at 52, 54 and 55 degrees are supposed to belong to the substrate.

XRD pattern shown in figure 37 (b) presents thin film prepared at voltage pulse length $\mathbf{t}_1$ = 50 μs, substrate heating **T** = 400 °C, average target power density

<S$_d$> = 13.0 W/cm^2 and deposition time **t** = 3000 s. The structure exhibits peaks of orthorhombic V_2O_5 at 20.3° (001) and 41.5° (002). Peaks at 10.6°, 21.3° (200) and 27.5° (103) are identified as tetragonal V_4O_9. Tetragonal VO_2 structure is indicated by peaks at 14.4° (110), 29.0° (220) and 44.3° (330). Peak at 69.0° belongs to Si substrate.

Figure 38 (a) shows structural and phase characterization of a thin film deposited at voltage pulse length **t$_1$** = 80 μs, substrate heating **T** = 400 °C and average target power density **<S$_d$>** = 13.9 W/cm^2 and time deposition **t** = 2700 s. In this sample only VO_2 structure was identified. The structure identification found tetragonal VO_2 at 27.8° (110), 39.8° (020) and weak peak at 57.4° (220). At the same positions could be identified monoclinic VO_2 (011), (020) or (002) and (022), respectively. The peak of Si substrate was identified at 69.0°. XRD pattern shown in figure 38 (b) describes a structure of the film deposited at the same deposition parameters as the previous one but time deposition **t** = 1350 s. Evidently this shorter deposition process produces a thinner film. This film exhibits weak peaks of VO_2 phase (tetragonal and monoclinic), which indicates worse crystallinity.

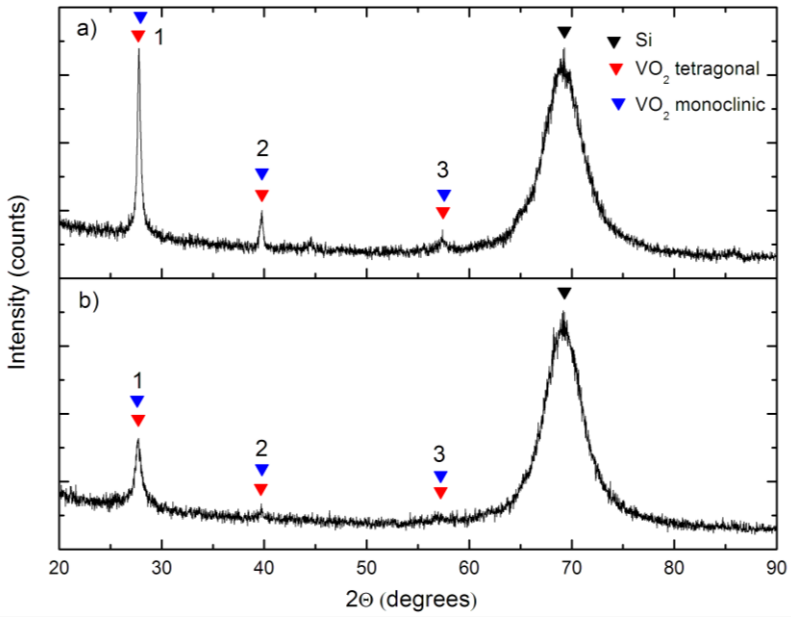

Fig. 38: XRD patterns of VO_2 thin films deposited at pulse length t_1 = 80 μs, average target power density <S_d> = 13.9 W/cm^2, substrate heating T = 400 °C and (a) deposition time t = 2700 s and (b) t = 1350 s. Crystallite orientation 1 – (110), 2 – (020), 3 – (220) for tetragonal VO_2 and 1 – (011), 2 – (020)/(002), 3 – (022) for monoclinic VO_2 thin film.

By reason of classifying prepared thin films into amorphous and crystalline groups as characterized by XRD, only crystalline thin films were analysed by Raman spectroscopy. Substrate heating **T** = 400 °C and average target power density **<Sd>** = 13.0 are uniform for all films. Obtained Raman spectra are shown in figure 39 indicating structure bonding in the crystalline thin films. These thin films deposited at voltage pulse length $\mathbf{t_1}$ = 40 μs, deposition time **t** = 1600 and 3200 s that are displayed in spectra (a) and (b), respectively, do not exhibit peaks belonging to VO_2. An analogical bonding structure is exhibited by Raman spectra (c) and (d), which were deposited at the voltage pulse length $\mathbf{t_1}$ = 50 μs, deposition time **t** = 1500 and 3000 s, respectively. However VO_2 peaks were identified in Raman spectra (e) and (f). Raman bands at 192, 222, 260, 308, 338, 388, 440, 495 and 612 cm^{-1}can all be assigned to vanadium dioxide. These thin films were prepared at the voltage pulse length $\mathbf{t_1}$ = 80 μs and deposition time **t** = 2700 and 1350 s.

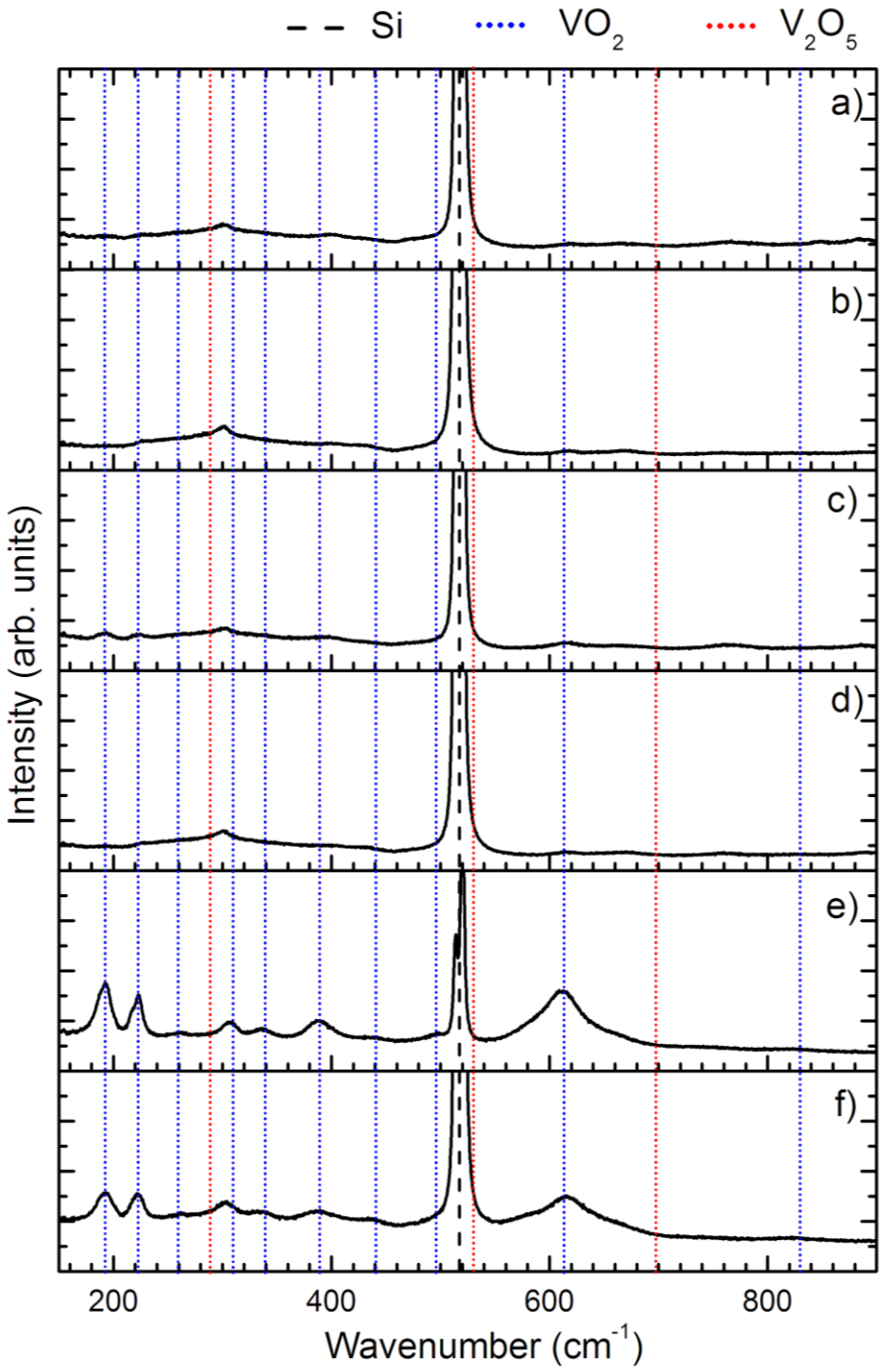

Fig. 39: Raman spectra for crystalline thin films. Raman bands for VO_2 are at 192, 222, 260, 308, 338, 388, 440, 495 and 612 cm^{-1}. Substrate heating T = 400 °C, <Sd > = 13.0 W/cm.^{2}(a) pulse length t_1 = 40 μs, deposition time t = 3200; (b) pulse length t_1 = 40 μs, deposition time t = 1600; (c) pulse length t_1 = 50 μs, deposition time t = 3000 s; (d) pulse length t_1 = 50 μs, deposition time t = 1500 s; (e) pulse length t_1 = 80 μs, deposition time t = 2700 s; (f) pulse length t_1 = 80 μs, deposition time t =1350 s.

5.4 THERMOCHROMIC PROPERTIES OF THE FILMS

Optical properties and characteristics are described in following section. Extinction coefficient, $\mathbf{k_{550}}$, and refraction index, $\mathbf{n_{550}}$, all samples are summarized in table 5.3 as well as thickness of the samples, which was evaluated by ellipsometric measurements.

Figure 40 illustrates a change of the ellipsometric angle $\Delta\mathbf{\Psi}$ as a function of film temperature. Amorphous films deposited without substrate heating (**T** < 40 °C) are represented by B curve (black) shown in the legend in figure 40. It can be seen no thermochromic behaviour at all because $\Delta\mathbf{\Psi}$ is kept at 0°. This is well supported by structure analyses in the previous section. Some films deposited at **T** = 400 °C and **<Sd>** = 13.0 W/cm^2 with a various voltage pulse length $\mathbf{t_1}$ and deposition time **t** exhibit similar evolution. These film's evolutions are represented by D (green), E (pink), F (orange) and G (violet) curves with deposition parameters: $\mathbf{t_1}$ = 50 μs and deposition time **t** = 1500 s, $\mathbf{t_1}$ = 50 μs and deposition time **t** = 3000 s, $\mathbf{t_1}$ = 40 μs and deposition time **t** = 1600 s, $\mathbf{t_1}$ = 40 μs and deposition time **t** = 3200 s, respectively. Nevertheless a strong thermochromic behaviour is clearly observed for VO_2 film prepared at $\mathbf{t_1}$ = 80 μs, **<Sd>** = 13.9 W/cm^2, **T** = 400 °C, deposition time **t** = 2700 and 1350 s. $\Delta\mathbf{\Psi}$ increases from 0° to 17.5°.

Tab 5.3: Characteristic parameters

Frequency f (Hz)	Pulse length t_1 (μs)	Heating T (°C)	$<S_d>$ (W/cm^2)	Thickness h (nm)	Refraction index n_{550} (-)	Extinction coefficient k_{550}(-)
125	80	< 40	14.0	77	2.17	0.19
		400	-	68	2.68	0.52
		< 40	13.9	143	2.24	0.14
		400	13.9	97	3.29	0.19
200	50	< 40	13.1	77	2.07	0.23
		400	13.0	64	2.12	0.58
		< 40	13.0	134	2.27	0.10
		400	13.0	103	2.35	0.33
250	40	< 40	12.4	80	1.95	0.32
		400	13.1	58	2.15	0.66
		< 40	13.2	122	2.34	0.08
		400	13.0	73	2.72	0.30

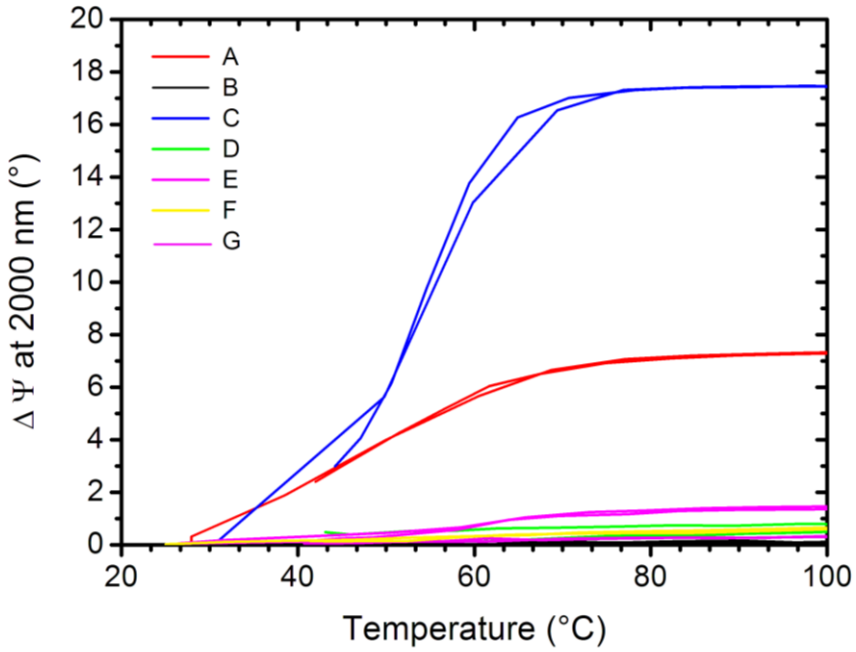

Fig.40: Temperature influence on a change of ΔΨ. Deposition parameters <Sd > ~ 13.0 W/cm^2, T = 400 °C; A: t_1 = 80 μs, t = 2700 s; B: amorphous films T < 40 °; C: t_1 = 80 μs, t = 1350 s; D: t_1 = 50 μs, t = 1500 s; E: t_1 = 50 μs, t = 3000 s; F: t_1 = 40 μs, t = 1600 s; G: t_1 = 40 μs, t = 3200 s.

Refraction index **n** and extinction coefficient **k** as a function of wavelength are illustrated in figure 41. It describes thermal behaviour of the film deposited at $\mathbf{t_1}$ = 80 μs, **<Sd >** = 13.9 W/cm^2, **T** = 400 °C and deposition time **t** = 2700 s. Figure 41 (a) shows refraction index **n** at different temperatures (25 – 100 °C). Evolutions for all temperatures show increasing of refraction index **n** with increasing wavelength from 300 to 450 nm. For longer wavelengths the refraction index **n** decreases only at temperature 25 and 50 °C. The other evolutions of refraction index **n** for temperatures 60, 70 and 100 °C decrease until wavelength 1480, 1025 and 1050 nm, respectively. The reason, why the films at temperatures 25 and 50 °C show different evolution than the higher wavelengths, can be explained by structural modification overcoming transition temperature $\mathbf{T_C}$.

Increasing temperature of the films evokes decreasing of a refraction index for all wavelengths in range of 300 – 1400 nm approximately. Significant influence of film temperature on refraction index is noticed at wavelength 1020 nm. Refraction index decreases from **n** = 3 (25 °C) to **n** = 1.6 (100 °C). On the other side, the films show a minimal dependence of a refraction index on film temperature at wavelength about 430 nm when refraction index drops from **n** = 3.7 to (25 °C) to **n** = 3.2 (100 °C).

Evolutions of extinction coefficient **k** as a function of wavelength at different film temperatures are shown in figure 41 (b). One can clearly see increasing evolution of extinction coefficient with increasing wavelength from 620 nm upwards. Simultaneously extinction coefficient **k** grows along with increasing film temperature (25 → 100 °C). This behaviour is very important regarding to thermochromic materials. Increasing film temperature strongly affects extinction coefficient, therefore absorption of radiation increases as well as increasing extinction coefficient **k**. The significant growth of extinction coefficient from **k** = 0.4 (25 °C) to **k** = 4 (100 °C) is at wavelength 1850 nm. This demonstrates successful fabrication of thermochromic VO_2 thin film, which reduces transmittance of infrared radiation for higher temperatures.

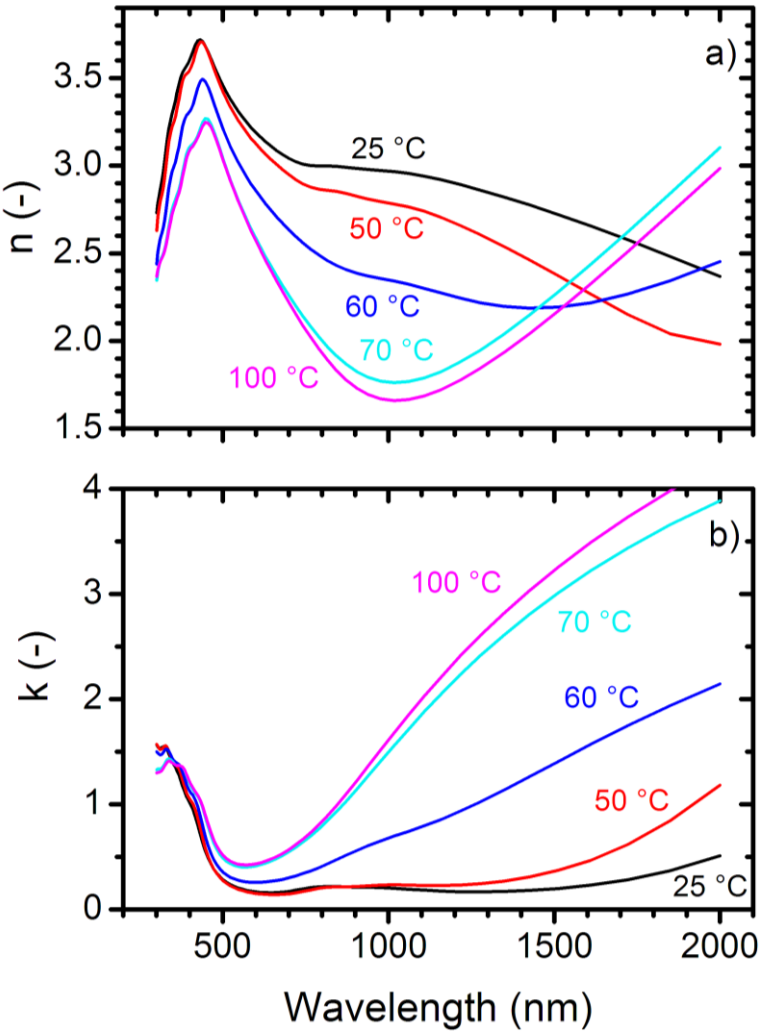

Fig.41: Optical parameters of the film prepared at t_1 = 80 μs, <Sd> = 13.9 W/cm^2, T = 400 °C, t = 2700 s. Refraction index (a) and extinction coefficient (b) of the film as a function of wavelength at different film temperatures.

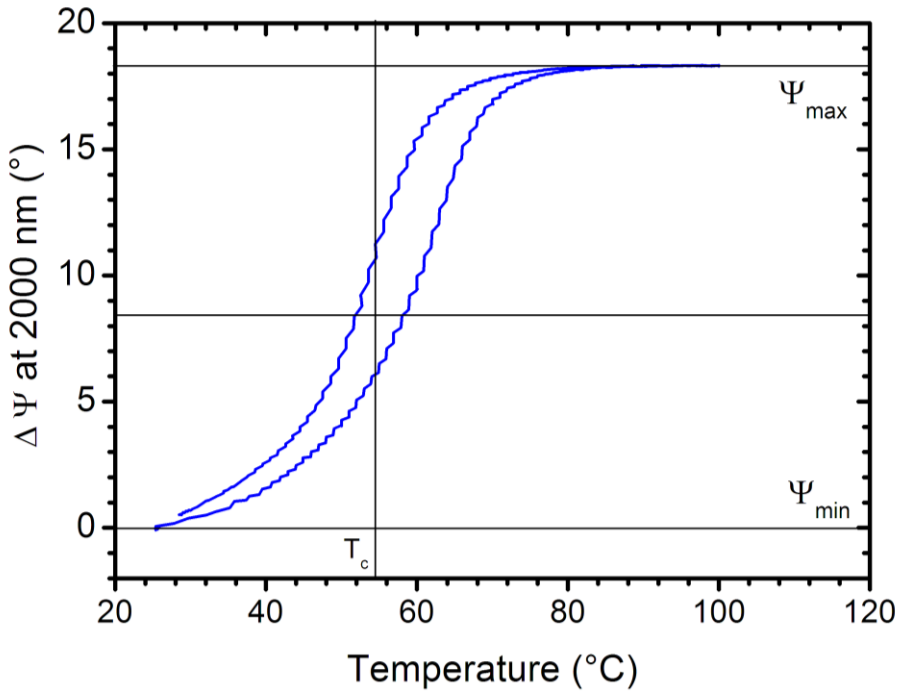

Fig. 42: Hysteresis behaviour of VO_2 film at 2000 nm. Heating rate = 1°C/min. The film was prepared at t_1 = 80 μs, <Sd> = 13.9 W/cm^2, T = 400 °C, t = 2700 s.

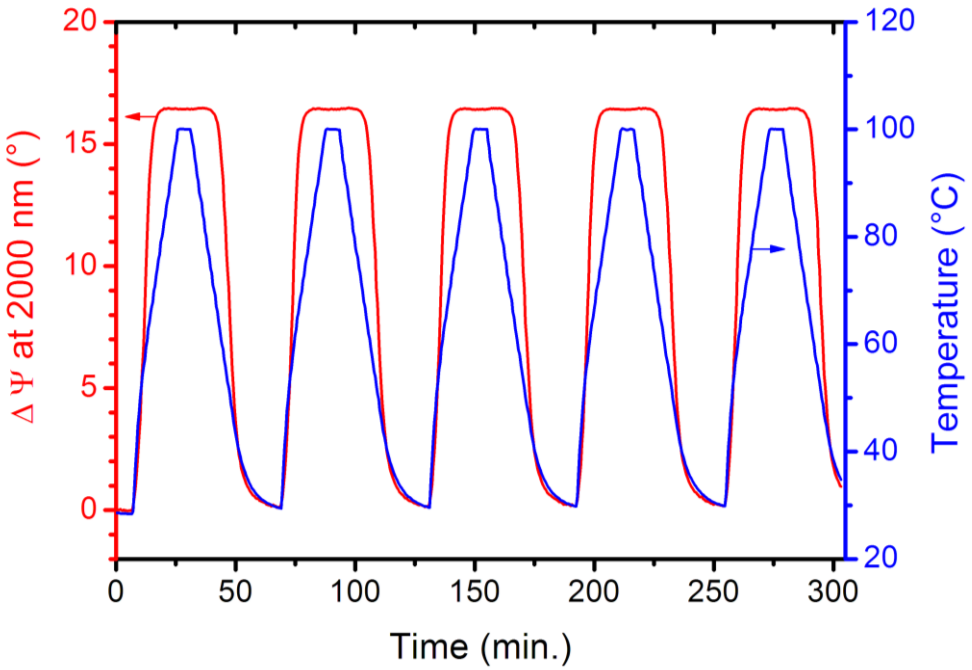

Fig. 43: Dependence of Δ Ψ on periodic thermal loading. The film was prepared at t_1 = 80 μs, <Sd> = 13.9 W/cm^2, T = 400 °C, t = 2700 s.

Figure 42 illustrates the hysteresis of the film prepared at $\mathbf{t_1}$ = 80 μs, **<Sd>** = 13.9 W/cm^2, **T** = 400 °C, **t** = 2700 s. Transition temperature $\mathbf{T_c}$ = 55 °C was evaluated in half of width of hysteresis loop at $0.5(\mathbf{\Psi_{max} - \Psi_{min}})$ as shown in the figure. The width of the hysteresis loop is 7 °C. The abrupt variation of $\Delta\mathbf{\Psi}$ indicates a crystalline structure in the film, which is in agreement with XRD pattern in figure 38.

A cycling change of film temperature is illustrated in figure 43. An intention of this measurement was to determinate thermochromic behaviour after a periodic thermal loading of the prepared film. The characteristic in figure 43 clearly shows periodic evolution of $\Delta\mathbf{\Psi}$ in five cycles, which refers to perfect reversible behaviour in time and in thermal changes. In order to accomplish this measurement a new film was sputtered to avoid possible thermal damage in previous optical measurement, which resulted in hysteresis. Deposition parameters stayed unchanged, $\mathbf{t_1}$ = 80 μs, **<Sd>** = 13.9 W/cm^2, **T** = 400 °C, **t** = 2700 s.

CHAPTER 6: CONCLUSION

The aims of this thesis are progressively realized in individual chapters of the thesis. First aim, doing research about present problematic of vanadium oxide and its preparation is described in the first chapter. The other aim is to deepen knowledge of high power impulse magnetron sputtering and related issues such as reactive magnetron deposition, arcing, hysteresis, self-sputtering etc. This aim is described in the second chapter. The fourth chapter is focused on the experimental system and techniques for preparation and analysis of thin films at the Department of Physics. The third aim of the thesis is realized in this chapter and it was also accomplished by personal participation in preparation of the thin films and evaluation of the results that are presented in the fifth chapter. The last aim is described in the fifth chapter - finding a relation among parameters of magnetron discharge, deposition characteristics and nature of sputtered films.

XRD Structural and phase analyses show a significant influence of substrate heating on the final structure of the films. Films that were prepared at the ambient temperature of substrate show no crystal structure therefore no thermochromic nature. On the other hand the films heated up to **T** = 400 °C show a crystal structure but VO_2 films were identified only on samples deposited at the voltage pulse length $\mathbf{t_1}$ = 80 μs and average power density **<Sd>** = 13.9 W/cm^2. It is known [47] that the main factors that affect the thermochromic performance are crystallinity and grain size. Therefore the need for higher substrate temperature during deposition process can be explained by a condition for crystallization, which allows forming crystalline VO_2 phase.

Raman and XRD structure analyses indicate high stoichiometric phases (V_2O_5, V_4O_9) of the films deposited at voltage pulse length $\mathbf{t_1}$ = 40 and 50 μs. Possible reason of this unwanted stoichiometry is an excessive amount of oxygen in RGFC controlled process. At the voltage pulse length $\mathbf{t_1}$ = 80 μs the amount of oxygen in the film was reasonable to form VO_2. This issue proposes sputtering thin films at the constant voltage pulse length and variable reactive gas flow in order to investigate the particular effect of amount of oxygen in films.

Ellipsometric measurements give excellent results confirming thermochromic nature of the film prepared at $\mathbf{t_1}$ = 80 μs, **<Sd>** = 13.9 W/cm^2, **T** = 400 °C, **t** = 2700 s. The thickness of this film was **h** = 97 nm. Extinction coefficient increases with increasing film temperature for wave lengths of infrared radiation. Significant growth of extinction coefficient is from **k** = 0.4 (25 °C) to **k** = 4 (100 °C) at wavelength 1850 nm. Transition temperature of the film is $\mathbf{T_c}$ = 55 °C, which is about 13 °C less than for bulk VO_2 ($\mathbf{T_c}$ = 68 °C). Thermochromic behaviour of the film is fully reversible. It is also important to note that this lowering of the transition temperature was achieved without any additive doping of the film. The film prepared at the same deposition parameters except deposition time **t** = 1350 s (thickness **h** = 68 nm) doesn't show such excellent results. This indicates another important factor – thickness that affecting thermochromic behaviour of VO_2 films. As shown in XRD analyses, thick film exhibits better crystallinity, which is the reason of better thermochromic behaviour.

REFERENCES

[1] M.E.A. Warwick, R. Binions. *Journal of Solid State Chemistry* Vol. 214. (2014). 53–66.

[2] Kiri, P.; Hyett, G.;Binions, R. *Adv. Mat. Lett*. 2010, 1(2), 86-105.

[3] Mott, N., F. *Reviews of Modern Physics*. 1968, 40(4), 677.

[4] Sparks, J.T.; Komoto, T. *Physics letters* A. 1967, 25(5), 398.

[5] Goodenough, J.B., *Journal of Solid State Chemistry*. Vol. 3(4), 1971, 490.

[6] Saeli, M. et al. *Energy and Buildings.* Vol. 42 (2010) 1666–1673.

[7] Gallardo-Amores, J.M. et al. *Chemistry of Materials*. Vol. 19(22) 2007, 5262-5271

[8] Kumar, A. et al. *Thin Solid Films*, Vol. 516, (2008) 912-918.

[9] F. Guinneton et al. *Journal of Physics and Chemistry of Solids*. Vol. 62. (2001) 1229 – 1238

[10] R.T. Kivaisi, M. Samiji. Solar *Energy Materials & Solar Cells*. Vol. 57 (1999) 141-152.

[11] N. R. Mlyuka, G.A. Niklasson, C.G. Granqvist. *Solar Energy Materials and Solar Cells.* Vol. 93. (2009).1685–1687.

[12] J.-P.Fortier et al. *Solar Energy Materials & Solar Cells*. Vol 125. (2014). 291–296.

[13] M.A. Sobhan et al. *Solar Energy Materials and Solar Cells*. Vol. 44 (1996) 451-455.

[14] W. Burkhardt et al. *Thin Solid Films* 402 (2002) 226–231.

[15] Y. Jiazhen et al. *Thin Solid Films* 516 (2008) 8554–8558.

[16] J. Du et al. *Solar Energy Materials & Solar Cells* 95 (2011) 469–475

[17] C. Piccirillo et al. *Thin Solid Films* 516 (2008) 1992–1997

[18] Y. Muraoka et al. *Jurnal of Physics and Chemistry of Solids* 63. (2002). 965 – 967.

[19] M. Ohring, The Material Science of Thin Films (1992)

[20] Bauer, G., Szyska, B., Vergohl, M., Bandorf, R. *Vacuum.* Vol. 84 (2010) 1354–1359.

[21] Kelly, P.J., Arnell, R.D., *Vacuum* 56 (2000) 159 – 172.

[22] A. Anders, *Surf. Coat. Technol*. 205 (2011) S1–S9.

[23] J. Musil, P. Baroch, J. Vlcek, K. H. Nam, J. G.Han, *Thin Solid Films* 475 (2005) 208.

[24] J. Rezek, Ph.D. Thesis (2013)

[25] S. Kadlec, J. Musil, J. Vyskočil. Vacuum 37 (1987) 729 – 738.

[26] M. Vergöhl, N. Malkomes, T. Matthée, G. Bräuer. *Thin Solid Films*. Vol. 377–378. (2000) 43 – 47.

[27] A. Anders, Thin Solid Films 502 (2006) 22 – 28

[28] D. Kim, D. J. Economou, J. Applied Physics. 94 (2003) 2852.

[29] J. C. Sellers. *Surf. Coat. Technol*.91-95 (1997) 184- 188.

[30] I. Petrov, F. Adibi, J. E. Greene, L. Hultman, J.-E. Sundgren, *Appl. Phys. Lett.* 63 (1993) 36.

[31] K. Sarakinos, J. Alami, M. Wuttig. *Appl. Phys* 2007; 40(7): 2108–14.

[32] J. M. Schneider, W. D. Sproul, A. A. Voevodin, A. J. Matthews. *Vac. Sci Technol.* A 1997; 15(3): 1084–8.

[33] J.W. Bradley, S. Thompson, Y. Aranda Gonzalvo, Plasma Sources Sci. Technol. 10, 490 (2001)

[34] J.T. Gudmundsson. Vacuum 84 (2010) 1360–1364.

[35] V. Kouznetsov, K. Macak, J. M. Schneider, U. Helmersson, I. Petrov, *Surf. Coat. Technol*.122 (1999) 290–293.

[36] G. Y. Yushkov and A. Anders, IEEE Trans. Plasma Sci. 38, 3028 (2010)

[37] J. T. Gudmundsson, J. Alami, and U. Helmersson, *Surf. Coat. Technol*. 161, 249 (2002).

[38] M. Hála, J. Čapek, O. Zabeida, J.E. Klemberg-Sapieha, L. Martinu. Surface and Coatings Technology. Vol. 206, Is. 19–20. (2012) 4186–4193.

[39] D. Horwat, A. Anders. *J. Appl. Phys*. 108, 123306 (2010).

[40] N. Hosokawa, T. Tsukada, and H. Kitahara, Proceedings of the Eighth International Vacuum Congress, pp. 11–14.1980.

[41] A. Andres, J. Anderson. *J. Applied Physics*. 102 (2007) 113303.

[42] Lectures of Seminar on Plasma Processing 2015.

[43] A. Anders, *Appl. Phys. Lett.* 92 (2008) 201501.

[44] H. Tompkins, E. Irene. *Handbook of Ellipsometry*. New York: William Andrew Publishing, 2005.

[45] I. R. Lewis, H. Edwards. *Handbook of Raman Spectroscopy*. CRC Press, 2001.

[46] J. R. Hook, H. E. Hall. *Solid State Physics*. New York: Wiley, 1995.

[47] S.H. Chen, et al. *J. Appl. Phys. Lett*. 90 (2007) 101117.